iScience

CellPress
OPEN ACCESS

Review

Synthetic strategies for MOF-based single-atom catalysts for photo- and electro-catalytic CO_2 reduction

Xiao Liang,[1] Shufang Ji,[2,*] Yuanjun Chen,[3] and Dingsheng Wang[1,*]

SUMMARY

The excessive CO_2 emission has resulted in climate changes, which has threatened human existence. Photocatalytic and electrocatalytic CO_2 reduction, driven by wind electricity and solar energy, are feasible ways of tackling carbon dioxide emission, as both energies are clean and renewable. Single-atom catalyst (SAC) is a candidate owing to excellent electrocatalytic and photocatalytic performance. Methods for preparing an SAC by using metal-organic frameworks (MOFs) as support or precursors are summarized. Also, applications in energy conversion are exhibited. However, the real challenge is to improve the selectivity of catalytic reactions to yield higher value products, which is to be discussed.

INTRODUCTION

The current demand for fossil fuel is growing, resulting in an excessive emission of CO_2, the main greenhouse gas. It is the main challenge to effectively reduce the emission of CO_2 and convert CO_2 into accessible resources so as to reduce total carbon dioxide (Zhao et al., 2021; Zou et al., 2021). Finding alternative energy sources and utilizing clean energy to convert CO_2 into reusable chemical raw materials and fuel are common concerns in recent studies (He et al., 2020; Li et al., 2020a; Yang et al., 2018a, 2019). The progress in carbon dioxide reduction reaction is expected to solve the environmental problems caused by excessive carbon dioxide emission.

Currently, electricity and solar energy are two relatively easily available clean energy sources, and their applications in the field of carbon dioxide reduction have been extensively studied (Chen et al., 2020a, 2021a). Electrochemical and photochemical methods could realize the conversion of CO_2 at room temperature and atmosphere pressure with a good application prospect (Peng et al., 2018; Sun et al., 2019). Photocatalysts activate carbon dioxide molecules by highly active photoelectrons excited by absorbing optical energy (Hao et al., 2021), whereas electrocatalysis drives the transfer of electrons through voltage (Shah et al., 2021). Although different energies are used, the common goal is to activate carbon dioxide by the catalytic active sites to convert other forms of energy into chemical energy. In terms of electrocatalysis, a low overpotential means a lower electrolysis voltage, and a high current density means a higher catalysis rate, which are important factors affecting electrocatalytic performance that needs to be optimized (Deng et al., 2019; Kim et al., 2019; Ting et al., 2020). As for photocatalysis, the catalytic activity depends on the capability of creating electron-hole pairs, which is the key point to generate free radicals for subsequent reaction process (Chu et al., 2020). The separation of electron and hole reflects the photocatalytic performance (Luo et al., 2019; Wang et al., 2020c). Regardless of whether it is electrocatalysis or photocatalysis, the reduction reaction of carbon dioxide is quite complicated. A variety of different reduction products can be obtained thermodynamically ((Equations 1), (2), (3), and (4)). How to control and obtain a single product, or to obtain a product with higher economic benefits, is still a big challenge.

$$CO_2 + 2H^+ + 2e^- \rightarrow HCOOH \quad \text{(Equation 1)}$$
$$CO_2 + 2H^+ + 2e^- \rightarrow CO + H_2O \quad \text{(Equation 2)}$$
$$CO_2 + 6H^+ + 6e^- \rightarrow CH_3OH + H_2O \quad \text{(Equation 3)}$$
$$CO_2 + 8H^+ + 8e^- \rightarrow CH_4 + 2H_2O \quad \text{(Equation 4)}$$
$$2CO_2 + 12H^+ + 12e^- \rightarrow C_2H_4 + 4H_2O \quad \text{(Equation 5)}$$
$$2CO_2 + 12H^+ + 12e^- \rightarrow C_2H_5OH + 3H_2O \quad \text{(Equation 6)}$$

(Equations 1), (2), (3), (4), (5), and (6)

[1]Department of Chemistry, Tsinghua University, Beijing 100084, China

[2]Department of Chemistry, University of Toronto, Toronto, Ontario M5S3H6, Canada

[3]Department of Electrical and Computer Engineering, University of Toronto, Toronto, Ontario M5S3G4, Canada

*Correspondence: shufang.ji@utoronto.ca (S.J.), wangdingsheng@mail.tsinghua.edu.cn (D.W.)

https://doi.org/10.1016/j.isci.2022.104177

This is an open access article under the CC BY-NC-ND license (http://creativecommons.org/licenses/by-nc-nd/4.0/).

The proposed redox reactions are related to catalytic activation of CO_2, which might lead to different products.

Owing to its high atomic utilization and excellent catalytic efficiency, single-atom catalysts (SACs) have been extensively studied (Yang et al., 2021; Zhang et al., 2020a, 2020b). SACs integrate the characteristics of both homogeneous catalysts and heterogeneous catalysts. By adjusting the coordination environment of the active site, the electronic structure of the active sites is regulated, thereby improving the selectivity and catalytic activity of the catalytic reaction (Cheng et al., 2019; Gong et al., 2020; Hou et al., 2020a). According to the TSK model, single atom with lower coordination number is inclined to be more reactive for electrocatalysis. Besides, controllable electronic structure of the catalytic sites adjusts the energy level structure of semiconductor affecting the absorption of photons or the transition of electrons (Guan et al., 2021). Meanwhile, the antenna effect enables the accumulation of charges at the single atom, which is conducive to the separation of electrons and holes (Zhang et al., 2021d). The inherent properties of single atoms as mentioned are advantageous in the application of electrocatalysis and photocatalysis (Jiao and Jiang, 2019; Zhuang et al., 2020). The precise structure of SACs also provides ideas and directions for further catalyst design (Zhang et al., 2021c). However, owing to the high surface energy, the preparation and stabilization of SACs is a major challenge. To find how to avoid the agglomeration of single atoms remains a problem.

Metal-organic frameworks (MOFs) are the new types of porous materials with a rich and uniform channel structure and high specific surface area. An adjustable metal node and ligand structure provide plenty of coordination sites to stabilize single atoms. MOFs have become good platforms for building and designing single atoms (Huang et al., 2020). MOF-derived materials obtained by the pyrolysis treatment of MOFs inherit the pore structure, and abundant coordination sites of MOFs, meanwhile, improve the conductivity and stability of the material, expanding the application of MOF-based single atoms (Zhao et al., 2019). Also, the porous structure enables the MOFs to have excellent mass transfer performance. The adsorption of carbon dioxide and other molecules and active species in the reaction process facilitates its interaction with the catalytic sites. Simultaneously, metal nodes and organic ligands in certain series of MOFs have intrinsically electrochemical and photochemical activity (Ikreedeegh and Tahir, 2021). Therefore, MOFs are good platforms for constructing single-atom electrocatalysts and photocatalysts.

With MOFs as templates to synthesize SACs, currently, the utilization of SACs in electrochemical and photochemical catalytic reduction of carbon dioxide has made progress (Figure 1). In this review, we will summarize the common strategies for applying MOFs to fabricate SACs, and elaborate these strategies in the catalyst construction process, combining them with advantages and characteristics exhibited in the photo/electro-catalytic carbon dioxide reduction reaction. Finally, the prospects and challenges of MOF-based methods in CO_2 photo/electro catalysis field will also be proposed.

STRATEGY FOR SAC SYNTHESIS AND APPLICATION IN CO2RR

MOF-based strategy and application in photocatalytic CO_2RR

As precursors of SACs, MOFs contribute to single-atom site separation, stabilization, and functional realization. Organic ligands, metal nodes, and pore structure are the three elements of MOFs. The coordination unsaturated non-metal atoms existing in the organic ligands of the framework and metal clusters at metal nodes could stabilize the single atom through coordination interactions. The pores with a specific size could wrap the precursors of a specific diameter, thereby realizing the separation of single atoms in space. The construction of MOF-based SACs will be introduced through three aspects below. For the photocatalytic CO_2RR, the conjugated pi-system in MOFs could absorb photons to realize the conversion of light energy into chemical energy. For the electrocatalytic CO_2RR, the graphene-like structure obtained by the pyrolysis of MOFs improves the electrical conductivity of the materials. The selection of MOFs and synthesis strategies has different emphases for photocatalysis and electrocatalysis, respectively. SACs for photocatalysis are mostly prepared using light-responsive MOFs. Also, the treatment is relatively mild to ensure that the photosensitive domains are not destroyed. SACs used for electrocatalysis require more severe treatment to obtain carbon materials with better conductivity.

Organic ligand stabilization strategy

The organic ligands in the MOF framework have a large number of coordination unsaturated non-metal atoms. Abundant coordination sites are utilized to capture precursors to achieve spatial dispersion and

CellPress
OPEN ACCESS

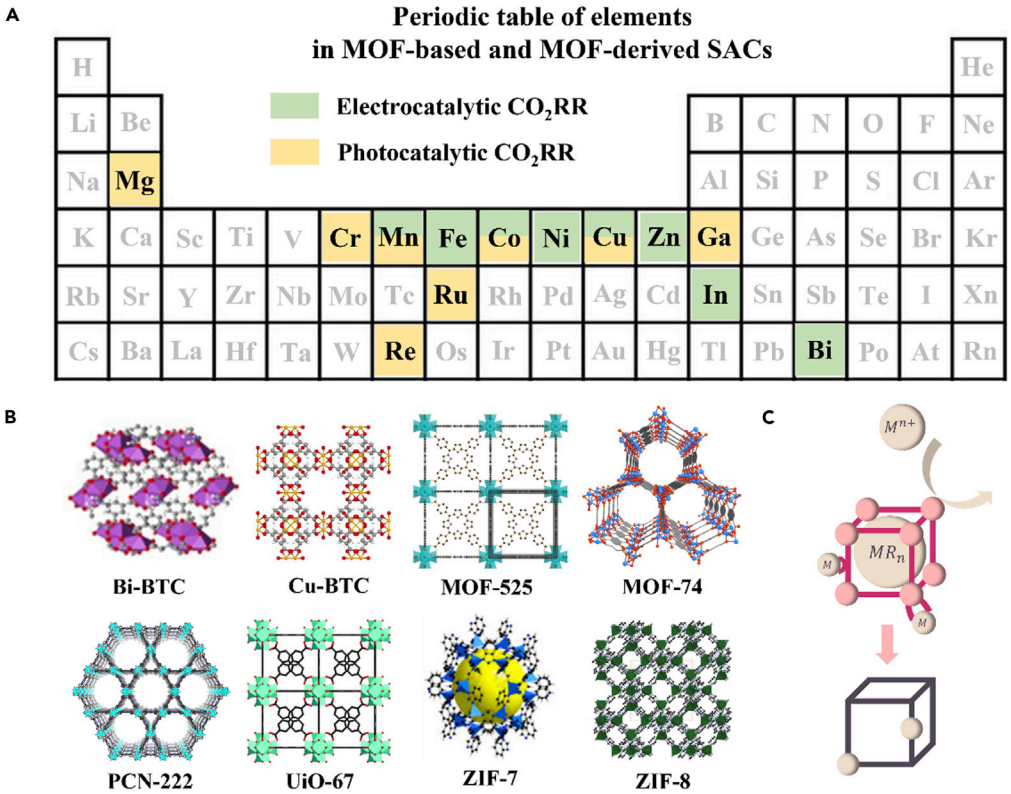

Figure 1. Summary of metal elements and MOFs for preparation of SACs

(A) Elements of MOF-based and MOF-derived SACs for electrocatalytic (green) and photocatalytic (yellow) CO_2RR.

(B) The structure of MOFs as precursors for SACs.

(C) Schematic illustration of strategies for preparing SACs using MOFs as precursors.

stabilize ultimate single metal atoms. Besides, a well-defined geometric structure and chemical coordination environment are conductive to determining the structure of the catalytic active sites, which is essential for explaining the reaction mechanism and further design optimization.

Wang and collaborators utilize ligand-stabilizing strategy to prepare Cu SACs for selective photoreduction of CO_2 (Wang et al., 2020a). Copper nitrate pentahydrate, used as the precursor of Cu species, is added into the suspension of pre-prepared UiO-66-NH_2. Cu precursor is captured by -NH_2 groups so as to realize the initial spatial separation of the Cu single atom. In contrast to the usual pyrolysis method, the photoinduced approach is adopted here, and the original spatial structure with abundant pores is maintained to a large extent with the utilization of light induction method, which is much milder than heat treatment. Through the interaction of the Cu and N atoms of the organic framework, a two-coordinated planar structure is formed, which stabilizes the single Cu atom (Figure 2A). No significant changes in photocatalytic activity and material structure are observed during the performance testing, demonstrating the stability of Cu SAs/UiO-66-NH_2. Compared with pristine MOFs, the Cu single atom doped material performs better in photocatalysis. The introduction of copper atom tunes electron structure of semiconductor. With lower conduction band energy, Cu-SAC possess narrower band gap, which is conducive to the enrichment of photoelectron (Figures 2B and 2C). The valence state of Cu atoms changes after light treatment, indicating the electron transfer towards Cu atomic sites (Figure 2D). In comparison with original MOFs in which photoelectron is enriched to the metal nodes, Cu-SAC performs with a higher efficiency of charge separation that is beneficial for the activation of CO_2. The energy barrier of the formation of COOH* that is considered as vital intermediate in CO_2RR is much smaller than other catalysts (Figure 2E), originating from the transformation of the electron-level structure caused by the introduction of the Cu atom and interaction between intermediate and amino groups through a hydrogen band. Reactive intermediate CO* and CHO* derived from COOH* further couple to generate ethanol, promoting the selectivity for CO_2RR towards ethanol.

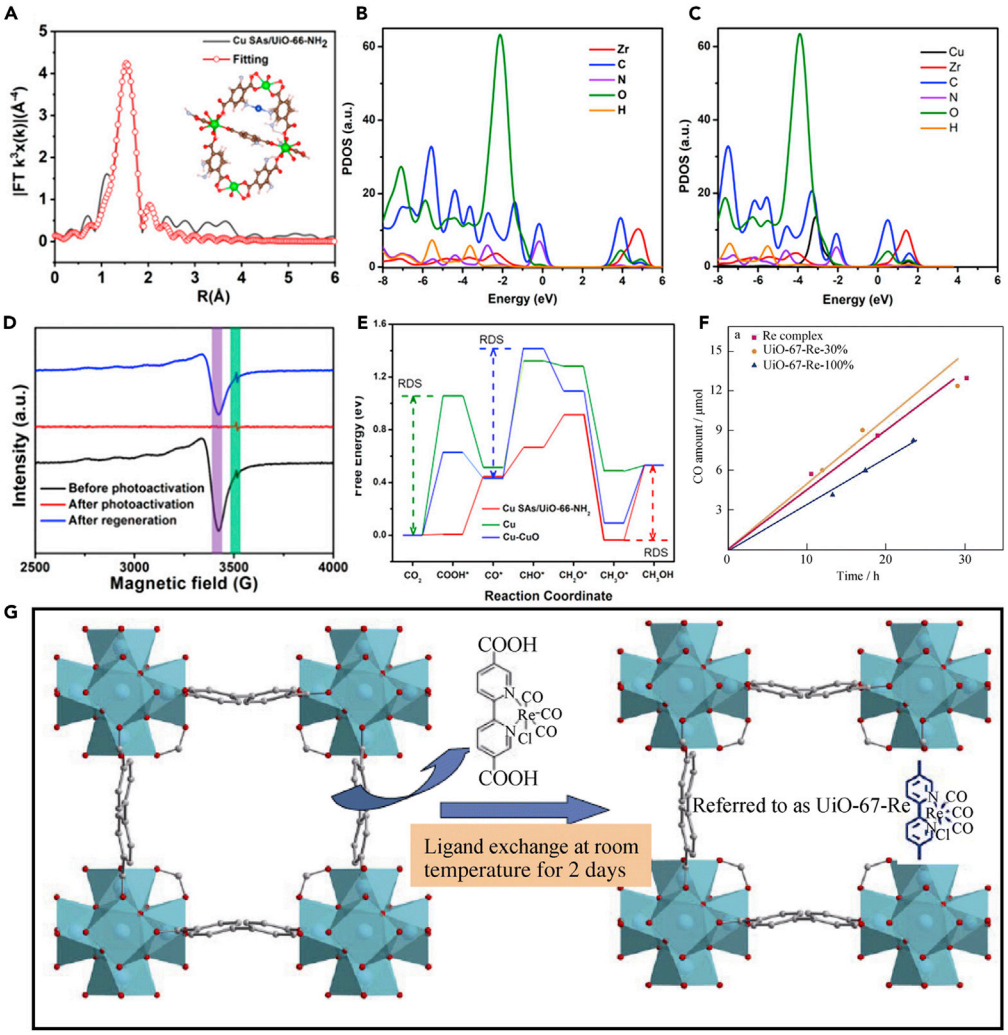

Figure 2. Synthesis and characterization of SACs prepared through an MOF-based strategy

(A) EXAFS fitting curves of Cu SAs/UiO-66-NH_2 at R space showing the coordination of Cu site. Reprinted with permission from Wang et al. (2020a) Copyright 2020 American Chemical Society.

(B and C) As-calculated partial density of states (PDOS) of UiO-66-NH_2 (B) and Cu SAs/UiO-66-NH_2 (C), which shows the narrow-band gap contributed from the Cu SAs. Reprinted with permission from Wang et al. (2020a) Copyright 2020 American Chemical Society.

(D) Low-temperature X-band EPR spectra of Cu SAs/UiO-66-NH2 showing valence changes of Cu occurring during the photocatalytic activation. Reprinted with permission from Wang et al. (2020a) Copyright 2020 American Chemical Society.

(E) Calculated free energy diagram of steps for CO_2RR showing a smaller energy barrier in the formation of *COOH in the case of Cu SAs/UiO-66-NH_2. Reprinted with permission from Wang et al. (2020a) Copyright 2020 American Chemical Society.

(F) CO yield of photocatalytic CO_2RR in the presence of Re-SAC with different contents of Re. Reprinted with permission from Chen et al. (2019) Copyright 2019 Springer Nature.

(G) Schematic of the preparation of Re-SAC by ligand exchange. Reprinted with permission from Chen et al. (2019) Copyright 2019 Springer Nature.

Chen and collaborators utilize the strategy of exchange after the construction of MOFs to fabricate Re-SAC for the photoconduction of CO_2 (Chen et al., 2019). A type of Re complex, the analogue of organic ligand of selected MOFs, is used as the Re precursor. An exchange with skeleton results in the introduction of Re species into MOFs. The framework has no significant change after ligand exchange. Through the control of exchanging time, a catalyst with different content of Re species is available (Figure 2G). By comparison of the CO-producing rate between the catalysts with different Re loadings, it is observed that the complete exchange for Re complex is not the optimal choice (Figure 2F).

Organic ligands of skeleton provide abundant coordination-unsaturated non-metallic atoms, which could ensure the stabilization of active metal atom through coordination interactions. By controlling the amount of precursors added, the amount of metal atoms in the active center that is finally loaded on the MOF can be adjusted. When an insufficient amount of metal precursors is injected, parts of organic ligands that are not coordinated will be retained, leading to accessibility to coordinate another species of metal atom, which results in the composition of different active species.

Liu and collaborators utilize a two-step self-assembly method to construct a Ru/Co bases catalyst (Liu et al., 2019). In the process of constructing MOFs, Ru species is first introduced. A special Ru precursor $Ru(H_2bpydc)(bpy)_2$ is used, containing the same structural unit as the organic ligand H_2bpydc in the MOFs, so that the Ru precursor can be assembled into the MOFs as a part of the framework. By adjusting the ratio of the added organic ligand and the Ru precursor, it is possible to achieve the adjustment of Ru loading. The part of the skeleton constructed by H_2bpydc contains N atoms without coordination saturation, which could stabilize the Co precursor subsequently injected into the system through coordination. The loading of Co also varies with the concentration of the added Co ion solution (Figure 3A). Thereby, MOFs loaded with two different metal atoms are obtained, exhibiting excellent photocatalytic activity for water splitting and CO_2RR, which can realize the preparation of water gas effectively. The ratio of reduction product H_2 to CO changes with the adjustment of the water content in the substrate CH_3CN/H_2O (Figure 3B) or the Co/Ru ratio of MOF-based catalysts. In the test of stability, $(Co/Ru)_{2.4}$-UiO-67(bpydc) shows no change in the photocatalytic activity after three cycles (Figure 3C), indicating stability for photocatalysis. Efficient photocatalytic performance comes from the integration of photosensitizer and catalytic active sites, promoting intramolecular transfer of the excited electron and separation of electron-hole pairs (Figure 3D). Diatomic site MOF-based catalyst demonstrates greater photocatalytic efficiency compared with a homogeneous system composed of two ions, which shows weak electron transfer from the photosensitizer to Co active sites with a similar potential.

Metal node stabilization strategy

The metal node should sum up several different strategies. What is common for these strategies is that the single atom is stabilized near the metal node of MOFs. It is easy to mistakenly think that a metal-metal bond is formed.

The metal node strategy also utilizes non-metal atoms with coordination ability, but it is different from the organic ligand stabilization strategy mentioned above. The metal nodes located on the surface of the material are different from those located in the body. The metal nodes on the surface with unsaturated coordination will be supplemented by the -OH/-OH_2 groups that exist in the system. These inorganic groups can act as multidentate ligands. They can be used to stabilize metal monoatomic species. Unlike organic ligands, this inorganic bridging ligand has differences in the structure and properties. Therefore, classifying it separately to distinguish it from organic ligands is more conducive to understanding its structure–activity relationship.

Abdel-Mageed and collaborators used the defect sites formed during the synthesis of UiO-66 to stabilize the Cu single atom (Abdel-Mageed et al., 2019). In the process of self-assembly of metal ions and organic ligands, linker mismatches might occur. Zr_6 clusters will capture other molecules or ions in the reaction system to form terminal structures containing defective sites, thereby providing unsaturated coordination sites, which could be used to stabilize single atoms. The Cu precursor was added to the MOFs that contain defects. The stable structure of the Zr oxide cluster is obtained by the solvothermal method. The post-treatment method of H_2 reduction is used to remove the coordinated and bound chlorine atoms on Cu. So, the Cu single-atom active sites can be fully exposed, showing excellent catalytic activity.

Among the metal node stabilization strategies, another strategy is essentially the exchange reaction of metal species. The node metal and the target metal undergo an ion exchange reaction. Single atoms replaced the original metal to become the new nodes. The target metal is doped into the framework of the MOFs, thereby realizing the spatial pre-separation of the metal atom.

Geng and collaborators utilize node metal ion exchange strategy to prepare an Sn-doped ZIF-8 (Geng et al., 2020). The doping method is also a good method for introducing two metals at the same time. By adjusting the degree of ion exchange, the ratio of introduced metal species could be easily regulated.

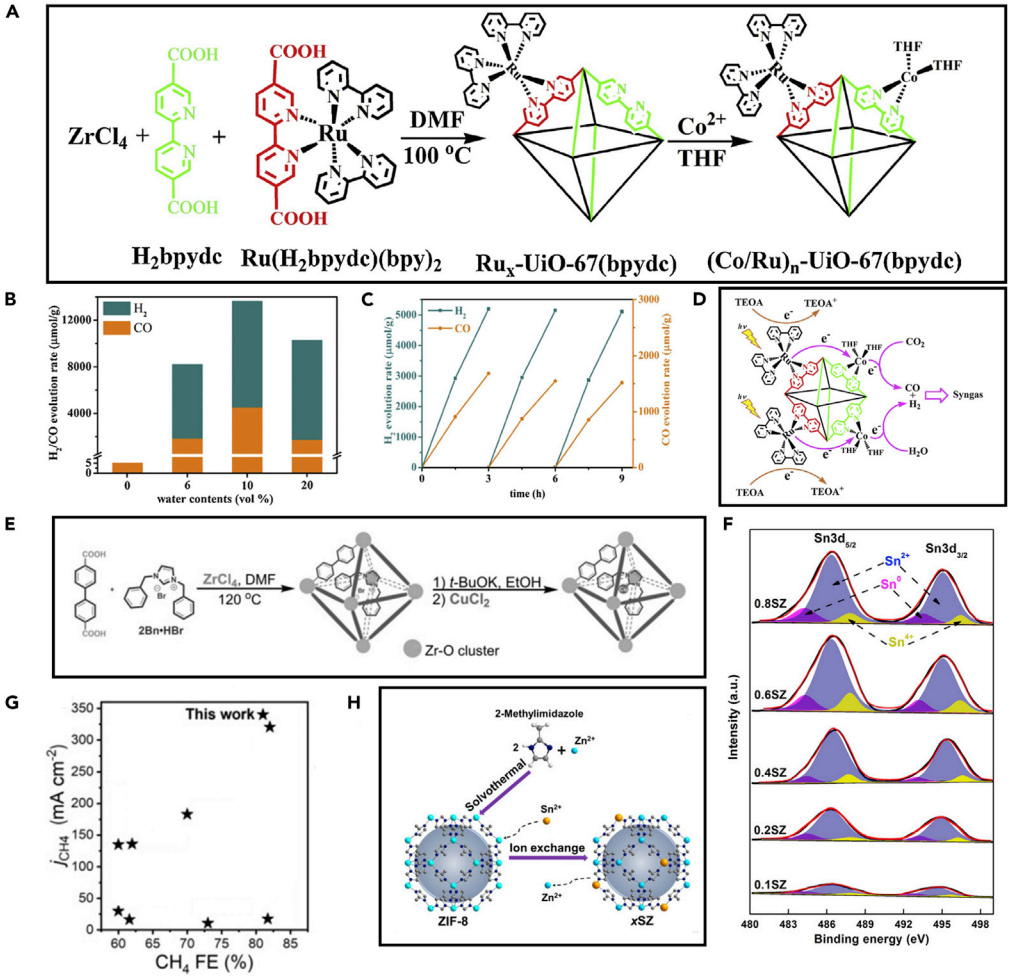

Figure 3. Preparation and characterization of an MOF-based single-atom catalyst

(A) Illustration of the synthetic process of Co/Ru-SAC. Reprinted with permission from Liu et al. (2019) Copyright 2019 Elsevier B.V..

(B) H_2/CO evolution rate at different H_2O contents. Reprinted with permission from Liu et al. (2019) Copyright 2019 Elsevier B.V..

(C) H_2/CO evolution rate through multiple catalytic cycles showing nearly no decrease in activity. Reprinted with permission from Liu et al. (2019) Copyright 2019 Elsevier B.V..

(D) Schematic of the proposed mechanism of photocatalytic production of syngas. Reprinted with permission from Liu et al. (2019) Copyright 2019 Elsevier B.V..

(E) Schematic of the preparation of SAC 2Bn-Cu@UiO-67. Reprinted with permission from Chen et al. (2022) Copyright 2021 Wiley-VCH GmbH.

(F) Sn 3-day XPS spectra of Sn-ZIF-8 with different tin contents. Reprinted with permission from Geng et al. (2020) Copyright 2020 Wiley-VCH Verlag GmbH & Co. KGaA, Weinheim.

(G) Electrocatalytic performance of 2Bn-Cu@UiO-67 showing the high current density and selectivity to CH_4. Reprinted with permission from Chen et al. (2022) Copyright 2021 Wiley-VCH GmbH.

(H) Schematic of the preparation of Sn-doped ZIF-8. Reprinted with permission from Geng et al. (2020) Copyright 2020 Wiley-VCH Verlag GmbH & Co. KGaA, Weinheim.

Through the self-assembly of Zn^{2+} and imidazole, the MOFs are first prepared. The prepared ZIF-8 powder is dispersed in an Sn^{2+}-containing methanol solution through a solution immersion method to obtain a tin-doped ZIF-8 through the exchange reaction of tin ions and zinc ions (Figure 3H). ZIF-8 doped with different tin contents could be prepared by adjusting the concentration of the tin ion solution (Figure 3F). The doping of tin ions does not damage the skeleton structure of ZIF so that the prepared catalyst effectively retains the topological structure and physical properties of the MOFs. At the same time, the introduction of new metals has improved the activity and selectivity of the CO_2 catalytic reduction.

CellPress
OPEN ACCESS

It is worth noting that there is a strategy to modify the metal nodes. Different functional ligands are connected to the metal nodes to provide new unsaturated coordination sites. The newly added organic ligands are used to stabilize the single atom through coordination. From the perspective of construction, this strategy is similar to the strategy of using inorganic bridging ligands, but in terms of functionality, it is more similar to the stabilization strategy using the organic ligands. The introduction of new ligands can enrich the functionality of materials that have stronger functionality and variability; thus, it is not limited only to the organic ligands in the framework

Pore confinement strategy

MOFs are porous materials with abundant pore structures having a uniform and adjustable pore size. When the size of the pore matches the diameter of the metal complex ion, the precursor could be added during the construction and growth of MOFs, so that the complex ion would be imprisoned in the cage of MOFs. Owing to the similar diameter, at most ,only one ligand ion could be confined in the pore at the same time, thereby realizing the pre-separation of the metal precursor. However, post-treatment is required later. In a relatively mild pyrolysis process, the precursor is decomposed without destroying the overall skeleton structure of MOFs. Also, the single atom would interact with the ligands to be stabilized. Therefore, the strategy of pore confinement is a pre-separation method that reduces the metal agglomeration during the heat treatment process through spatial separation.

Chen and collaborators adopt several kinds of organic ligands matching the diameter of the MOFs pore (Chen et al., 2022). The separation of the metal active site is achieved by pore restriction. The radius of the organic ligand is close to that of the pore, so that only one ligand can be contained in the same pore. The realization of this strategy benefits from the precise control of the pore structure of MOFs. The metal salts are then added to the system, and immobilized in the pores of MOFs through coordination with the organic ligands that are previously confined in the pores (Figure 3E). Testing CO_2RR performance, it exhibits high catalytic activity and good selectivity, which could be reflected by the current density and Faraday efficiency (Figure 3G).

Photocatalytic CO_2RR

In the photocatalytic reduction process, the adsorption and activation of carbon dioxide is still an important part of the catalytic reaction. The porous structure of MOFs, with more exposure of active sites on the surface, makes it easier to capture carbon dioxide.

Photocatalytic activity depends on the ability of the catalyst to absorb light and create electron-hole pairs (Angulo-Ibanez et al., 2021). Broadening the wavelength range of light that the catalyst can absorb, increasing the intensity of light absorption, and promoting the separation of electron-hole pairs are the common approaches to improve the performance of photocatalysts.

The process of photocatalytic reduction often involves the participation of multiple electrons, molecules, and active intermediates, so the selectivity of the product is relatively difficult to control.

Huang and collaborators took advantage of the highly dispersed active sites of SACs. The catalytic reactions were carried out in independent active sites and accordingly through the unimolecular reaction path, thus eliminating the interference of multi-molecular reactions and achieving good product selectivity (Huang et al., 2016). The Re-SAC is constructed through the strategy of ligand stabilization. The ligands bound with Re ions and $ZrCl_4$ are mixed and react to obtain SACs with Re atoms coordinated on the skeleton (Figure 4A). They use longer length ligands to achieve sufficient separation of the Re active sites in space, thereby ensuring the independence of the catalytic sites in the catalytic process. It ensures that the catalytic reaction proceeds through a single-molecule process, realizing the efficient conversion from carbon dioxide into carbon monoxide (Figure 4B). The transformation of coordination structure of the active site could be inferred through the changes of vibrational frequencies of ligand CO (Figure 4C). With LED as the light source, the metal-to-ligand charge transfer (MLCT) occurs. The catalyst enters the preparatory state for CO_2 activation. However, the MLCT of Re-SAC is a single-electron process, which is insufficient for the two-electron process of CO reduction. It is necessary to add triethylamine as the electron donor to provide a second electron owing to the separation of Re sites.

Fei and collaborators also use ligand stabilization strategies, but they use post-processing methods (Fei et al., 2015). First, the organic ligand is mixed with the corresponding metal salt by the general method

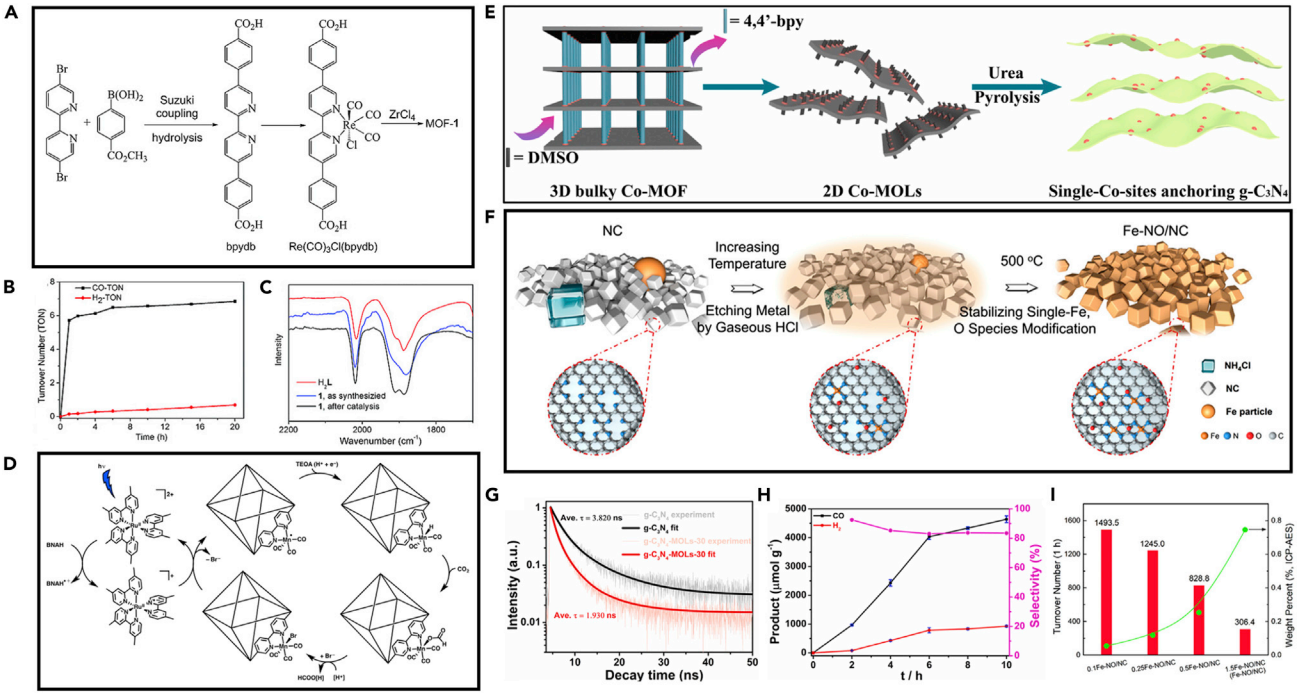

Figure 4. Preparation of SACs and application in photocatalytic CO_2RR

(A) Diagram of the preparation of Re-SAC. Reprinted with permission from Huang et al. (2016). Copyright 2016 Wiley-VCH Verlag GmbH & Co. KGaA, Weinheim.

(B) The TON curves of the two reduction products varied with the catalytic reaction time reflecting the durability and selectivity of catalyst. Reprinted with permission from Huang et al. (2016). Copyright 2016 Wiley-VCH Verlag GmbH & Co. KGaA, Weinheim.

(C) FTIR spectra of Re-SAC before and after catalysis. Changes of vibrational frequencies of the carbonyl groups showing the variation of coordination of Re site. Reprinted with permission from Huang et al. (2016). Copyright 2016 WILEY-VCH Verlag GmbH & Co. KGaA, Weinheim.

(D) Scheme of the proposed mechanism of the formation of the formate from photocatalysis. Reprinted with permission from Fei et al. (2015) Copyright 2015 American Chemical Society.

(E) Schematic of the synthesis of Co-C_3N_4 through pyrolysis of MOFs. Reprinted with permission from Zhang et al. (2021a) Copyright 2021 Elsevier Ltd.

(F) Schematic of the preparation of Fe-N_4O through a post-processing strategy. Reprinted with permission from Li et al. (2020c) Copyright 2020 American Chemical Society.

(G) Time-resolved photoluminescence spectra of Co-C_3N_4 and C_3N_4. Reprinted with permission from Zhang et al. (2021a) Copyright 2021 Elsevier Ltd.

(H) CO and H_2 yield and selectivity of Co-C_3N_4. Reprinted with permission from Zhang et al. (2021a) Copyright 2021 Elsevier Ltd.

(I) Turnover count of a series of catalysts with different contents of Fe species. Reprinted with permission from Li et al. (2020c) Copyright 2020 American Chemical Society.

to prepare MOFs. The ligand in the framework contains abundant coordination unsaturation sites. The prepared MOFs are dispersed with ether, and then Mn precursor ions are added. Through the coordination of organic ligands and Mn ions, Mn-SAC supported by MOFs is prepared. Because the Mn-CO bond in the precursor $Mn(CO)_5Br$ is relatively weak, the complex can be decomposed and bound to the organic ligand under relatively mild solvothermal conditions. The obtained catalyst can specifically reduce carbon dioxide to formate, and the selectivity could reach about 96%. Although Mn-based catalysts are chosen to replace precious metals, a small amount of Ru complexes are still needed as photosensitizers during the reaction (Figure 4D). Mn-SAC itself could not respond to light. Photosensitizer is required to activate the single-atom sites.

Zhang and collaborators use node stabilization strategy to fabricate SACs (Zhang et al., 2021a). The researchers chose a cobalt-containing MOFs as precursors. Through the exchange between solvent molecule and organic ligand, the MOFs are stripped from the bulk to obtain two-dimensional layered MOFs. Co-SAC supported by C_3N_4 was prepared by pyrolysis. Urea is added as a supplementary nitrogen source during heat treatment (Figure 4E). Compared with pristine C_3N_4, Co-SAC exhibits more efficient charge separation under photoexcitation. According to the time-resolved photoluminescence spectra, Co-C_3N_4 displays reduced average exciton lifetime, ensuring better charge transfer performance

Table 1. Representative examples of SACs with MOFs as precursors for photocatalytic CO_2RR

Catalyst	Precursor	Synthesis strategy	Main product	Product rate/ TON	Medium	Illumination	Reference
Co-MOF	MOF-525	Ligand stabilization	CO	200.6 μmol g^{-1} h^{-1}	MeCN/TEOA = 4:1	400 nm < λ < 800 nm (300 W Xe)	(Zhang et al., 2016)
Co-MOF	MOF-525	Ligand stabilization	CH_4	36.67 μmol g^{-1} h^{-1}	MeCN/TEOA = 4:1	400 nm < λ < 800 nm (300 W Xe)	(Zhang et al., 2016)
Cr-UiO-66	UiO-66	Ligand stabilization	HCOOH	11	MeCN/TEOA = 4:1	420 nm < λ < 800 nm (300 W Xe)	(Lee et al., 2015)
Ga-UiO-66	UiO-66	Ligand stabilization	HCOOH	6	MeCN/TEOA = 4:1	420 nm < λ < 800 nm (300 W Xe)	(Lee et al., 2015)
Cu-UiO-66	UiO-66	Ligand stabilization	CH_3OH	5.33 μmol g^{-1} h^{-1}	0.5 M Na_2SO_4	λ ≥ 400 nm (300 W Xe)	(Wang et al., 2020a)
Cu-UiO-66	UiO-66	Ligand stabilization	C_2H_5OH	4.22 μmol g^{-1} h^{-1}	0.5 M Na_2SO_4	λ ≥ 400 nm (300 W Xe)	(Wang et al., 2020a)
Mg-TiO_2	MIL-125	Node stabilization	CO	12.6 μmol g^{-1} h^{-1}	Gaseous phase	450 W Xe	(Feng et al., 2020)
Mn-UiO-67	UiO-67	Ligand stabilization	$HCOO^-$	50 ± 7.8	DMF/TEOA = 4:1	470 nm LED (ThorLabs, Inc.)	(Fei et al., 2015)
Re-PMOF	PCN-222	Ligand stabilization	CO	1893	DMF	λ > 500 nm (450 W Xe)	(Choi et al., 2021)
Re-MOF	MOF-1	Ligand stabilization	CO	6.44	MeCN/H_2O/TEA	410 nm LED	(Huang et al., 2016)
Re-MOF	UiO-67	Ligand stabilization	CO	0.09	MeCN/Et_3N	400 nm < λ < 700 nm (300 W Xe)	(Choi et al., 2017)
Ru-PCP	UiO-67	Ligand stabilization	HCOOH	40.3	MeCN/TEOA	385 nm < λ < 740 nm (300 W Xe)	(Kajiwara et al., 2016)
Ru-MOF	MOF-253	Ligand stabilization	$HCOO^-$	35.8	MeCN/TEOA = 10:1	Visible light	(Sun et al., 2015)

(Figure 4G). Co-SAC shows high photocatalytic activity and good selectivity for carbon monoxide (Figure 4H).

Li and collaborators synthesize Fe-SAC with the coordination of heteroatoms nitrogen and oxygen by the strategy of heteroatom trapping (Li et al., 2020c). ZIF-8 is served as the precursor of the N-doped carbon material. Through pyrolysis, Carbon material with a certain morphology and pore structure is obtained. Nitrogen could capture metal atoms through coordination. Commercial Fe particle is utilized as metal source. The HCl gas produced by the pyrolysis of NH_4Cl reacts with Fe particles to obtain volatile ferric chloride, which enters the carbon material by gas-phase diffusion and is captured by nitrogen atoms (Figure 4F). Eventually, the constructed active site structure Fe-N_4O of high valence iron would promote the absorption of the CO_2. Also, it shows high activity of photocatalytic CO_2RR with turnover up to 1,494 h^{-1} (Figure 4I). Representative examples of SACs for photocatalytic CO_2RR are summarized here (Table 1).

As for photocatalytic CO_2RR, reduction products are usually relatively simple preliminary reduction products such as CO, HCOOH, etc., and the specific selective reduction of more complex reduction products containing multiple carbon atoms is still a challenging subject to be studied.

Although solar energy, a relatively clean energy, is used for the photocatalytic CO_2RR, organic reagents are used as electron donors or sacrificial reducing agents in many systems, resulting in new problems in environmental protection.

MOF-derived strategy and application in electrocatalytic CO_2RR

As for MOF-based SACs, the porous topological structure brings good mass transfer efficiency. Optically active organic ligands could serve as photosensitizers. Therefore, the MOF-based strategy is often used to prepare photocatalysts. However, relatively poor resistance to harsh chemical environments and heat is the prevalent problem for MOFs, which restricts the application fields of MOF-based SACs. Poor electrical conductivity affects the application prospects for electrocatalysis. Through the post-processing of MOFs, a series of derivation of MOFs is fabricated. MOF-derived materials inherit the porous structure. Calcining process decomposes the organic component remaining inorganic constituent, which increases the heat stability and corrosion resistance. Widely applied N-doped carbon materials with similar structure

to graphene exhibits excellent conductivity expanding its application in the field of electrocatalysis (Cui et al., 2022; Han et al., 2021).

It is similar to the method of MOF-based decomposition of metal precursors, except that a higher decomposition temperature is used, so that the organic components of MOFs and the metal precursor are pyrolyzed. Finally, MOF-derived SACs are prepared. Metal species can be derived straightly from the metal nodes of framework or the addition of precursor. Owing to the use of higher temperatures during pyrolysis, the problem of aggregation of single metal atoms needs to be considered.

Organic ligand stabilization strategy

Owing to the use of higher pyrolysis temperature and more severe reaction conditions, metal agglomeration is more likely to occur. Therefore, it is particularly important to select the appropriate combination of ligand and metal precursor to stabilize the SACs. Generally, the ligand structure containing nitrogen and other heteroatoms with strong coordination ability could be used to form relatively stable N-coordinated metal single atom during the pyrolysis process, avoiding metal agglomeration under high temperature conditions.

Chen and collaborators utilize UiO-66-NH_2 as the precursor. W-SAC supported by N-doped carbon material is prepared (Chen et al., 2018). The UiO-66 material modified with amino group has an unsaturated coordinating amino group on the organic ligand, which plays an important role in stabilizing tungsten single atoms. The organic ligand is carbonized and decomposed at a high temperature, and the amino-coordinated tungsten species forms the structure of WNC_3 (Figure 5A). On the one hand, the organic ligand combines with the tungsten precursor to attain the pre-dispersion of the metal atom, and on the other hand, it also acts as nitrogen source for the decomposition product. During the pyrolysis, the organic component is carbonized to form a graphite-like structure, whereas the inorganic component forms the corresponding oxide. Also, the latter could be removed by hydrofluoric acid etching without affecting the structure of the carbon material. Thus, the N-doped carbon material that retains the original octahedral pore structure of MOFs could be obtained (Figure 5B). The excellent electrical conductivity of carbon materials enables the materials to have a wide range of applications in electrocatalytic reactions, whereas the porous structure and large specific surface area reduce the restriction of the mass transfer process on the reaction rate and catalyst performance.

Mixed metal node stabilization strategy

Zeolitic imidazolate frameworks (ZIFs) are one of the most widely used MOFs. With low-boiling-point metal Zn as metal nodes, the Zn component evaporates the remaining nitrogen and carbon elements during pyrolysis to form porous N-doped carbon material. So, ZIFs serves as model pre-support for fabricating MOF-derived SACs.

Chen and collaborators fabricate Fe-SAC utilizing MOF-derived strategy (Chen et al., 2020b). Through ion exchange, ferrous ion replaces the original Zn^{2+} at metal nodes of ZIF-8. Fe ions doped into skeleton keep certain spatial distance to realize the primary spatial separation of Fe species. With pyrolysis of ZIF, the organic ligand is carbonized and Zn component is volatilized. Finally, Fe species exist in the form of Fe-N_4 to generate Fe-SAC (Figure 5D). Because of different diffusion rates of two species of metal, the Kirkendall effect occurs and results in a mesopore structure of the obtained carbon material (Figure 5E). The prepared Fe SAC shows fine CO_2 reduction selectivity towards CO.

There are many contradictions in the selection of pyrolysis temperature and Fe loading. A high concentration of ferrous ion in the ZnFe-ZIF and high temperature for heat treatment will result in the aggregation of Fe species to nanoparticles. The low loading of Fe might affect current density, reducing the electrochemical performance. An inadequate heating temperature leads to an increase in residual Zn content and incomplete graphitization of the organic skeleton. The N-doped carbon structural unit synthesized at a low temperature decreases the selectivity of the CO_2 reduction reaction, owing to the competitive electrochemical reaction of HER. An appropriate choice of temperature and metal content is of great importance to electrocatalysts (Figure 5C).

Wen and collaborators fabricate the N-stabilized Ni metal catalyst by pyrolysis of Ni-MOFs (Wen et al., 2019). Pre-prepared Ni-MOFs are added into the solution of urea. The resulting suspension is stirred for

CellPress
OPEN ACCESS

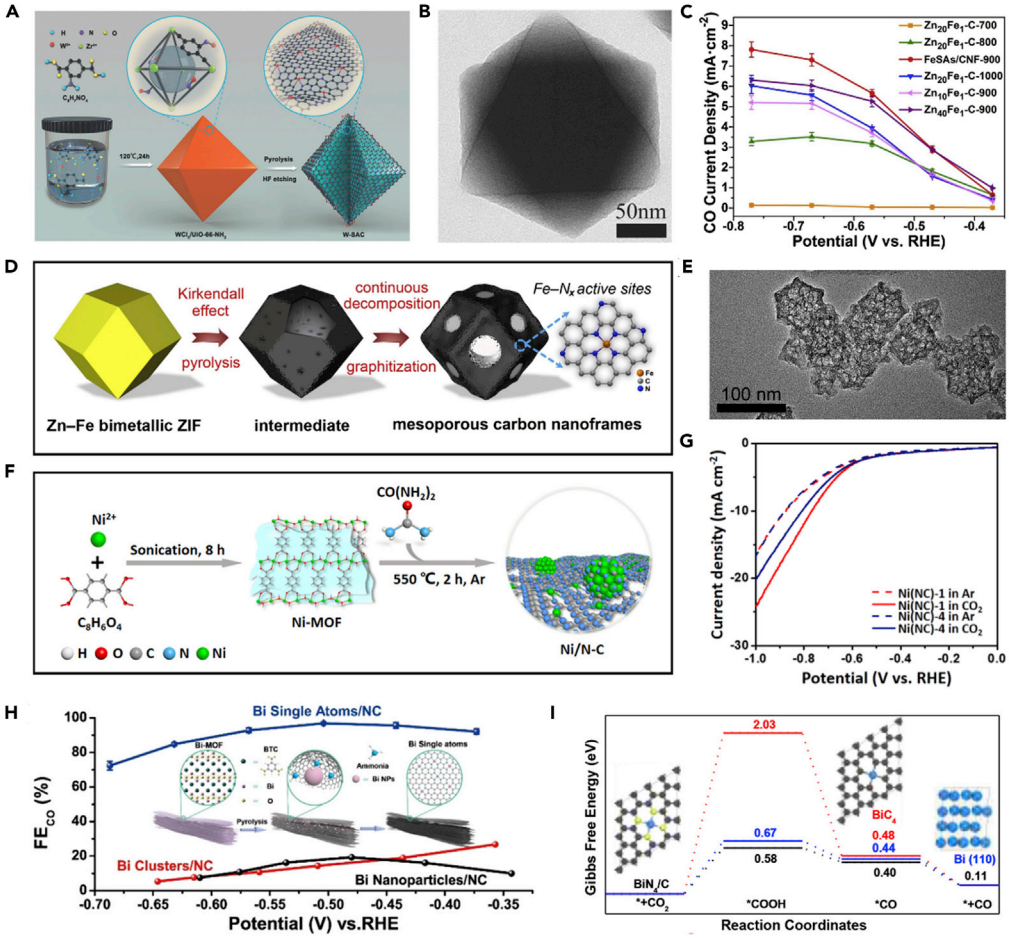

Figure 5. Fabrication and characterization of SACs prepared by an MOF-derived strategy

(A) Schematic illustration of preparation of W-SAC. Reprinted with permission from Chen et al. (2018) Copyright 2018 Wiley-VCH Verlag GmbH & Co. KGaA, Weinheim.

(B) TEM image of W-SAC. No sintering is observed after pyrolysis. Reprinted with permission from Chen et al. (2018) Copyright 2018 Wiley-VCH Verlag GmbH & Co. KGaA, Weinheim.

(C) Partial current densities of CO at different potentials for Fe-SAC prepared with different Zn/Fe ratios and pyrolysis temperatures. Reprinted with permission from Chen et al. (2020b) Copyright 2020 Elsevier B.V..

(D) Schematic of the preparation of Fe-SAC by pyrolysis of bimetallic MOFs. Reprinted with permission from Chen et al. (2020b) Copyright 2020 Elsevier B.V.

(E) TEM of Fe-SAC showing the mesopore structure of the carbon material caused by Kirkendall effect. Scale bar, 100 nm. Reprinted with permission from Chen et al. (2020b) Copyright 2020 Elsevier B.V..

(F) Schematic of the synthesis process of Ni/N-C. Urea served as a nitrogen source. Reprinted with permission from Wen et al. (2019) Copyright 2019 American Chemical Society.

(G) Comparison between the current density of Ni(NC)-1 and Ni(NC)-4. Reprinted with permission from Wen et al. (2019) Copyright 2019 American Chemical Society.

(H) Schematic of the preparation of Bi-SAC with bismuth transforming from nanoparticle to single atom and Faradaic efficiency of different catalysts. Reprinted with permission from Zhang et al. (2019) Copyright 2019 American Chemical Society.

(I) Calculated Gibbs free energy diagram for CO2RR with different catalysts showing the low-energy barrier for the formation of *COOH intermediate on Bi-SAC. Reprinted with permission from Zhang et al. (2019) Copyright 2019 American Chemical Society.

a period of time so that the urea could be well dispersed into the MOFs. The Obtained colloidal substance is freeze-dried to remove the solvent. Ni-MOF utilized here does not contain nitrogen, and the addition of urea serves as a supplement to the nitrogen source in the heat treatment process AFTERWARDS. Finally, the dried solid powder is put into the ZrO_2 boat for subsequent pyrolysis. And N-doped carbon material

loaded with Ni motifs is fabricated (Figure 3F). The prepared nitrogen-carbon materials have the same two-dimensional layered structure as the original MOF. Ni species anchored on the support comprise both atomically dispersed Ni and Ni metal nanoparticles that are stabilized through nitrogen coordination. Via adjusting the proportion of Ni-MOF and urea, material consisting of more components of Ni NPs is fabricated with more Ni-MOF added into the pyrolysis reaction. Ni(NC)-1 with less NP components performs with a higher Faradic efficiency for the conversion into CO, which exceeds 90% from potential −0.65 V to −0.90 V. After a 3-h catalytic performance test at optimal potential − 0.75 V, the current density of CO generation shows no invisible decrease, which manifests fine stability. By comparison between FE and j_{CO} of Ni(NC)-1 and Ni(NC)-4, two kinds of material with different Ni species as the precursor containing same Ni molar quantity but different content of Ni NPs, it provides experimental evidence for negative effects of the NP content (Figure 5G). Different species including single atoms and N-coordinated nanoparticles are introduced into the same system. By modulating the proportion of different Ni sites, the contribution to electrocatalysis is interpretated briefly. However, the non-uniformity of Ni species in the system presents difficulties in complaining the exact mechanism of electrocatalytic process. But deleting the postprocessing to remove the NPs simplifies the procedure, which greatly promotes the feasibility for a practical application.

Zhang and collaborators apply subsequent treatment to decompose the Bi nanoparticles into atomically dispersed Bi (Zhang et al., 2019). The obtained Bi-SAC performs well in electrochemical reduction of CO_2 towards CO. Given the vestige of Zn species during heat treatment of ZIFs, synthesis of MOF-derived Bi-SAC is put forward, utilizing Bi-base MOFs. Fasciculation-shaped MOFs are fabricated by the method of the solvothermal reaction. Subsequent pyrolysis does not completely change the morphology of material. With the increase of temperature of heat treatment, Bi atom migrate from metal nodes to assemble together to generate Bi nanoclusters. Along with the process of Ostwald ripening, Bi clusters in border position gradually aggregate into center position. Large-grained nanoparticles come into existence. The unwilling aggregation of the single atom occurs frequently during the pyrolysis of MOFs. The application of an ingenious method of atomization make Bi NPs return to an atomically dispersed state. Dicyandiamide pyrolyzed to release NH_3 is utilized as a nitrogen source. Nitrogen is finally implanted into the carbon layer to form a coordination site to capture and stabilize the evaporated Bi atom (Figure 5H). Spectroscopy measurement demonstrates the existence of Bi-N_4 sites with Bi atom at a low valence. Bi-N_4, as the catalytic active site, performs excellent selective CO2 electrochemical reduction to CO with the Faradic efficiency reaching 97% (Figure 5H). A high TOF and low overpotential are also reported. Going through DFT calculation illustration, outstanding catalytic activity is ascribed to lowest Gibbs free energy for generation of intermediate *COOH, which is the determining step for the activation of CO_2 (Figure 5I).

Pore confinement strategy

Spatial separation and coordination stability of non-metal elements are the two main ideas for constructing stable SACs. The pore confinement strategy belongs to the former, which uses the uniform-sized pore structure in the MOFs to provide steric hindrance so that the metal precursor can be pre-separated. After the pyrolysis, the organic components decompose, and the metal species in the pores are transferred to the derived carbon materials. Metal atoms are coordinated and stabilized by the nitrogen originated from the organic components. The content of the introduced metal species could be easily adjusted by the concentration of the metal precursor.

Zhao and collaborators prepare MOFs with a uniform pore structure by room temperature liquid-phase synthesis (Zhao et al., 2017). After dispersing the obtained ZIF-8 powder with n-hexane, an aqueous solution of nickel nitrate was added to disperse nickel ions into the pores of MOFs. The ZIF-8 with nickel ions is finally subjected to high-temperature pyrolysis. The volatile zinc component is vaporized and separated from the system at a high temperature. The organic component is pyrolyzed to form carbon material retaining the skeleton structure. Ni atom coordinates with the nitrogen atom produced by the decomposition of imidazole to form a relatively stable porphyrin-like structure (Figure 6A).

Derivative coordination site capture strategy

Different from the idea for preparing MOF-derived materials mentioned above, the metal of active site is introduced after the heat treatment of MOFs. Therefore, it is not necessary to consider whether the introduced metal precursor could always maintain single-atom dispersion under relatively severe conditions like pyrolysis. This post-processing method usually uses a top-down strategy (Xiong et al., 2021), which uses

CellPress
OPEN ACCESS

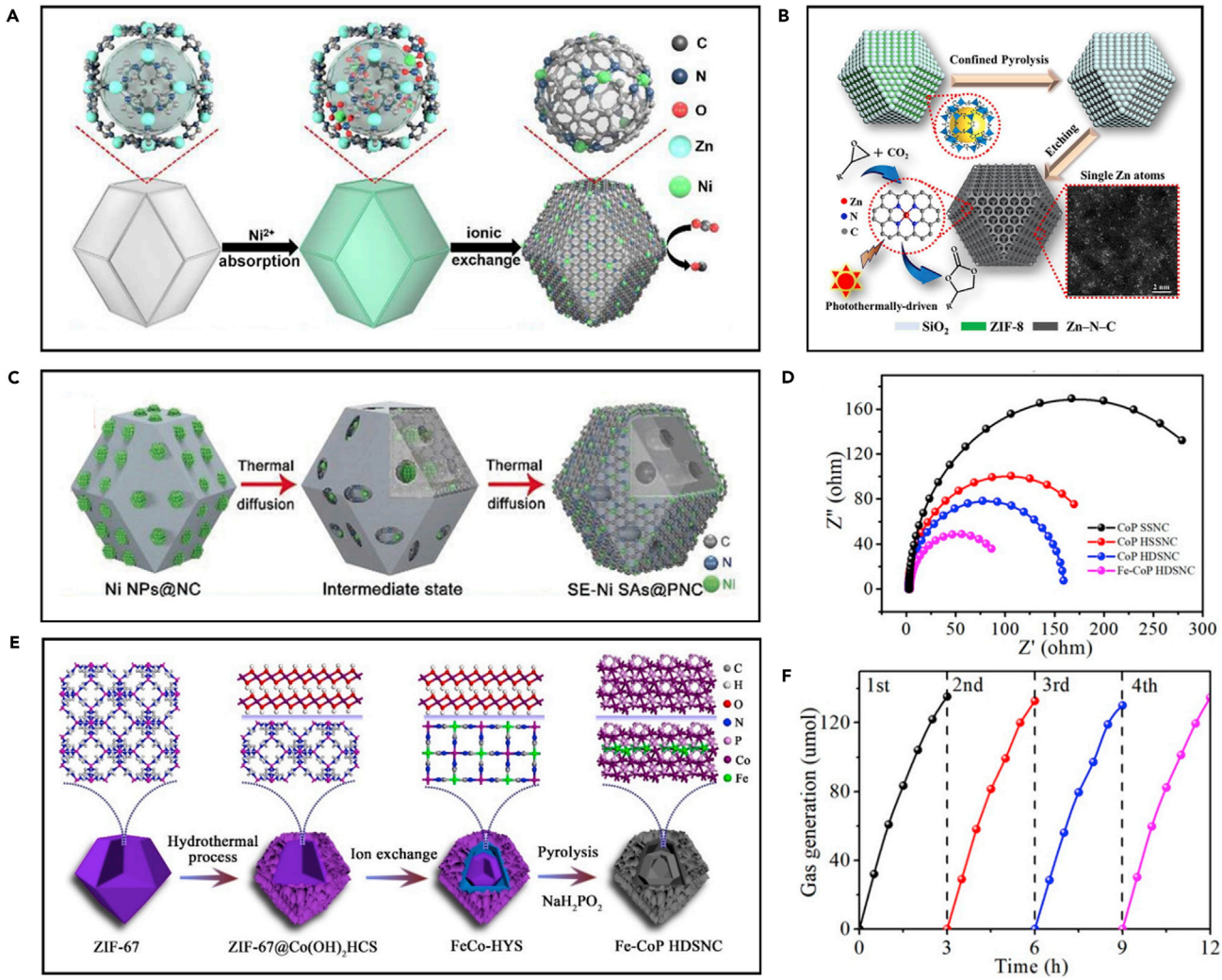

Figure 6. Synthesis and characterization of SACs prepared by an MOF-derived strategy

(A) Schematic of the formation of Ni-SAC. Precursor confined in the pore of MOFs. Reprinted with permission from Zhao et al. (2017) Copyright 2017 American Chemical Society.

(B) Schematic of the preparation of Zn-SAC. SiO_2, served as a template, is etched after pyrolysis. Reprinted with permission from Guo et al. (2020) Copyright 2020 Elsevier Inc..

(C) Illustration of synthesis of Ni-SAC. Reprinted with permission from Yang et al. (2018b) Copyright 2018 Wiley-VCH Verlag GmbH & Co. KGaA, Weinheim.

(D) Electrochemical impedance spectroscopy (EIS) of Fe-CoP. Fe-CoP shows the smallest semicircle diameter. Reprinted with permission from Wang et al. (2021a) Copyright 2021 American Chemical Society.

(E) Schematic illustration of the preparation of Fe-CoP. Reprinted with permission from Wang et al. (2021a) Copyright 2021 American Chemical Society.

(F) CO generation in the stability test showing almost no decay. Reprinted with permission from Wang et al. (2021a) Copyright 2021 American Chemical Society.

agglomerated nanoparticles as the metal precursor. The strong coordination and stabilization effect of non-metal atoms is used to form a stable metal single atom. There is no need to worry about the agglomeration of metal species into particles.

Yang and collaborators use N-doped carbon material produced by the decomposition of ZIF-8 as the carrier of the catalyst. Nickel nanoparticles supported by the carbon material are prepared through the reduction of nickel acetylacetonate (Yang et al., 2018b). Later, the agglomerated Ni nanoparticles are re-dispersed into a single-atom form by means of high-temperature treatment (Figure 6C). Comparing the adsorption energies of different nickel species under different coordination environments, it is shown that the structure of Ni-N_x(x = 3,4) has a lower adsorption energy. It explains the

thermodynamic stability of the SAC, which also provides theoretical explanation for the feasibility of top-down preparation strategy.

MOFs composite strategy

In addition to the corresponding MOFs derivatives generated by the pyrolysis of MOFs, a series of composite materials could be obtained by compounding MOFs with other functional materials. Currently, several materials are frequently used as candidates for composite materials, including the semiconductor, metal nanoparticles, and polymer materials (Chen et al., 2021b; Sun et al., 2021; Wang et al., 2022). They introduce different functionalities to MOF-based catalysts and provide new approaches for the synthesis of MOF-based catalysts.

Guo and collaborators exploit a new approach to synthesize MOF-derived N-doped carbon materials with a hierarchical porosity structure applied for the photoconversion of CO_2 (Guo et al., 2020). Pre-prepared nanosphere SiO_2 is dispersed into the solution of binder PVP to generate colloidal crystal template SiO_2. SiO_2-CCT is immersed into a system consisting of precursors of ZIF-8. MOFs grow in the interstice of SiO_2-CCT to form a coating structure. After heat treatment, ZIF-8 are converted into carbon material. Maintaining SiO_2-CCT as the core section is removed by immersion with the NaOH solution. In consequence, Zn atomically dispersed N-doped carbon material is obtained. During the pyrolysis, a relatively hard template of SiO_2-CCT prevents ZIF-8 from structural shrinkage caused by the decomposition of the organic ligand; thus, the mesoporous structure is retained. According to the analysis of the porous structure of obtained catalysts, two sizes of porosity coexist, which is conducive to mass transport. PVP with carbonyl group coordinating with Zn ions and organic ligand also facilitate the growth of ZIF-8. The porous material prepared above shows excellent performance for CO_2 cycloaddition with a yield of 95%. During the reaction process, N-coordinated Zn serves as active sites. Zn single atoms as Lewis acid and nitrogen as Lewis base constitute the nanoreactor. The material fabricated by etching after pyrolysis consists of abundant channels (Figure 6B), which plays a crucial part in light-harvesting and diffusion of reactant and product.

By wrapping hydroxide in the outer layer of MOFs, Wang and co-workers prepare a special double-shelled structure nanocages (Wang et al., 2021a). The single atomic metal sites are introduced through ion exchange. The inner MOFs and outside hydroxide both transform to CoP after the sequent treatment of low-temperature oxidation and phosphorylation, finally forming a hierarchical double-layer CoP nanostructure (Figure 6E). The special microstructure brings good mass transfer performance. According to the electrochemical impedance spectroscopy, Fe-CoP displays small charge-transfer resistance (Figure 6D) that contribute to its well photocatalytic CO_2RR activity. Fe-CoP also shows good stability during the durability test (Figure 6F).

Combining with other different materials to form a composite structure provides more ideas and possibilities for the preparation of SACs. Compared with single MOFs, the composite could provide richer spatial and topological structure, as well as diverse coordination environment.

Electrocatalytic CO_2RR

MOFs have poor stability under relatively harsh chemical conditions and poor electrical conductivity, which limits its application in electrocatalysis. However, through a high-temperature pyrolysis under the protection of inert gases, the organic components are carbonized to form carbon-based materials doped with heteroatoms such as nitrogen and oxygen (Gao et al., 2021; Zhou et al., 2021b). The graphite-like structure significantly improves the electrical conductivity of the materials, whereas the retention of spatial topology in the pyrolysis process makes the MOF-derived material still has good mass transfer performance (Li et al., 2020b).

Carbon dioxide is a relatively stable molecule, and the initial activation of carbon dioxide is often a key step in the reduction of carbon dioxide (Handoko et al., 2020; Hu et al., 2020). The initial activation of carbon dioxide in electrocatalytic reduction may go through the following three paths (Quan et al., 2021). These include two kinds of process of co-transfer of protons and electrons, and one involves only electron transfer without the participation of protons. At the same time, it may also involve the competitive side reaction of proton reduction (Equations 7, 8, 9, and 10). Different carbon dioxide activation pathways involve different reactive intermediates, which would affect the process of subsequent reduction reactions (Jing et al., 2021;

Zhang et al., 2021b). It ultimately leads to different selectivities of reduction products. This is the key to achieving efficient and selective reduction of carbon dioxide (Wang et al., 2021d). For traditional transition metal and post-transition metal catalysts, activation usually undergoes a process of co-transfer of proton and electron, whereas for homogeneous catalysts, the reaction path is different and usually involves only the activation process of electron transfer (Birdja et al., 2019). SACs are different from homogeneous catalysts and traditional heterogeneous catalyst systems in the structural characteristics of active sites, so they have different catalytic performance from traditional catalysts:

$$CO_2 + H^+ + * + e^- \rightarrow *COOH \quad \text{(Equation 7)}$$
$$CO_2 + H^+ + * + e^- \rightarrow *OCHO \quad \text{(Equation 8)}$$
$$CO_2 + * + e^- \rightarrow *CO_2^- \quad \text{(Equation 9)}$$
$$H^+ + * + 2e^- \rightarrow *H^- \quad \text{(Equation 10)}$$

Most of the carbon-supported SACs prepared with MOFs as the precursors have the active site structure of M-N_x. On account of the reduction of energy barrier of certain elementary steps, the reaction is more inclined to proceed in the corresponding path. The selectivity of the CO_2RR is thus increased. The electronic structure of the active site is related to its coordination environment, which could be regulated by introducing heteroatoms, etc. The adjustment of activity and selectivity could be achieved by such methods.

Theoretical tools such as DFT help to understand the relationship between catalytic selectivity and active site structures. It provides an approach for the comprehension of the process of catalytic reactions. And it also plays a significant role in the interpretation of the characterization results.

Pan and collaborators utilize the strategy of metal node stabilization. Zinc ions in the ZIFs are replaced by ferric ions, so that iron-doped MOFs are obtained (Pan et al., 2018). Through high-temperature pyrolysis in an inert atmosphere, zinc volatilized at high temperatures to obtain Fe-SAC supported by nitrogen-doped carbon materials. The Fe K-edge XANES characterization shows that the valence state of iron is between 2+ and 3+ (Figure 7A), and K-edge EXAFS infers the coordination structure of Fe-N_4 (Figure 7B). In the electrocatalytic reduction test, $KHCO_3$ is used as the electrolyte. Compared with the nitrogen-doped carbon material without metal loading, it has a more positive onset potential. In terms of product selectivity, the products are mainly carbon monoxide and hydrogen. No other reduction products such as hydrocarbons are detected. The Faradaic efficiency of carbon monoxide of Fe-SAC can reach 93% at an overpotential of 0.47 V, showing excellent reduction selectivity (Figure 7E). Through DFT calculation and simulation, it is found that the active site of Fe-N_{2+2}-C_8 structure containing carbon atoms with dangling bonds has an energy advantage in the decomposition process of COOH* active intermediates (Figure 7D).

Ye and collaborators adopt the strategy of ligand stabilization (Ye et al., 2016). Firstly, straight coordination between the ligand and the organometallic salt is used to prepare Re chelate. The two ends of the chelate contain coordination unsaturated hydroxyl groups, which can further interact with zinc ions so as to form the skeleton structure of MOFs. During this process, the coordination structure of Re remains unchanged, and Re SACs are obtained (Figure 7F). MOFs are also immobilized on the FTO (Fluorine doped tin oxide) glass electrode through the interaction of zinc ions and hydroxyl groups on the substrate. In terms of electrocatalytic reduction, the catalytic activation process is similar to that of homogeneous catalysts. Both involve the transformation process of the valence state of the central metal atom, which can specifically reduce CO_2 to CO. Its Faraday efficiency could reach 93% (Figure 7C).

Tan and collaborators adopt mixed metal node stabilization strategy mentioned above to synthesize Mn-SACs (Tan et al., 2021). The MOFs with Mn and Zn nodes were prepared by adding the organic ligand methylimidazole into the mixed solution of Mn and Zn salts. In the subsequent pyrolysis process, the Zn component volatilizes owing to its low boiling point. So, the SAC of Mn was obtained. Mercaptopropionic is added as the source of sulfur to realization the doping of sulfur atom. The introduction of heteroatoms adjusts the coordination structure of the active center and improves the reduction selectivity of the catalyst (Figures 7G and 7H). The sulfur atom could form an S-O bond with the oxygen atom in the active intermediate *COOH, which might delocalize the electron and stabilize the active intermediate (Figure 7I). Representative examples of SACs for electrocatalytic CO_2RR are summarized here (Table 2).

The activation process of carbon dioxide involves the chemical adsorption of carbon dioxide molecules on the surface of the catalyst. There exist differences in the activation process of carbon dioxide for

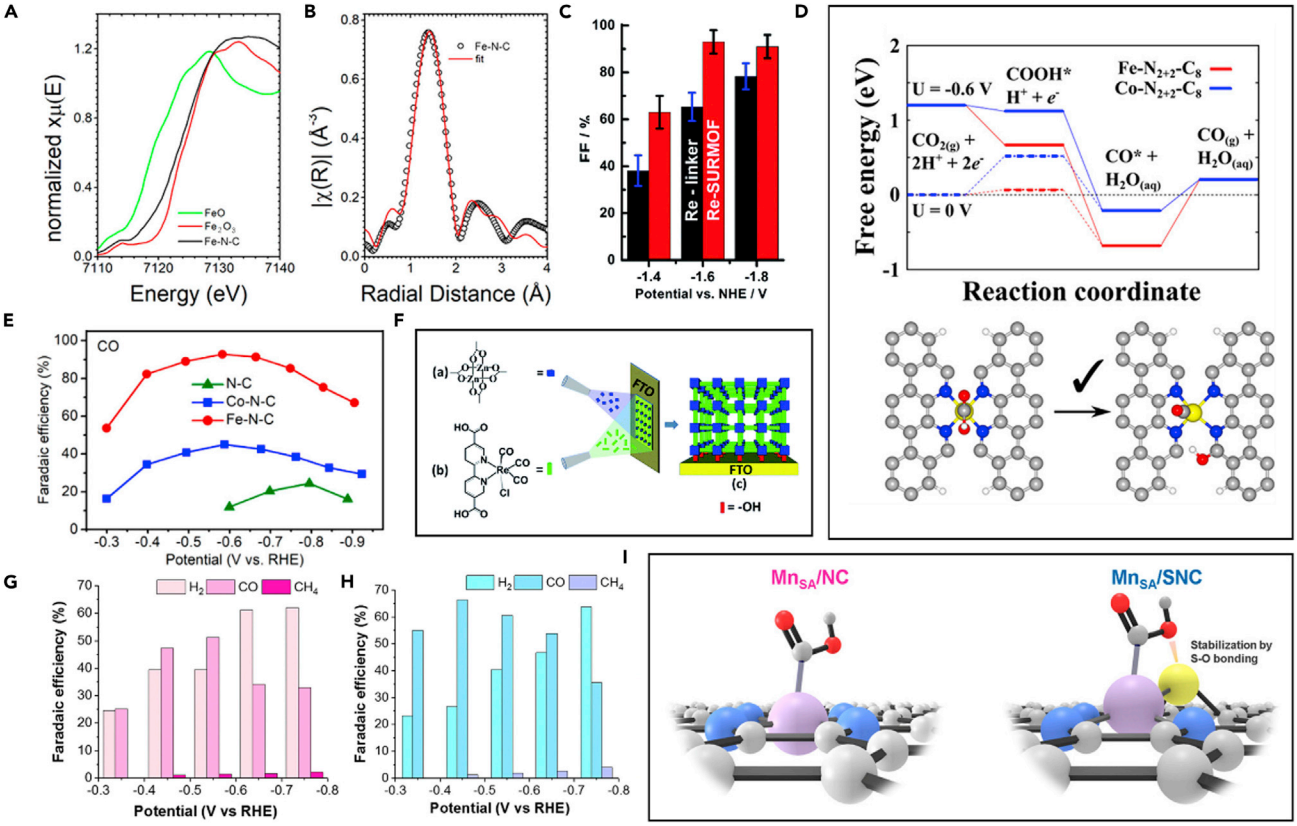

Figure 7. Preparation of SACs and application in electrocatalytic CO_2RR

(A) XANES curves of Fe K-edge showing the mediate valence state of Fe at active site. Reprinted with permission from Pan et al. (2018) Copyright 2018 American Chemical Society.

(B) EXAFS fitting curve of Fe K-edge showing the coordination. Reprinted with permission from Pan et al. (2018) Copyright 2018 American Chemical Society.

(C) Faradaic efficiency of Re-SAC at different potentials, showing good selectivity to CO. Reprinted with permission from Ye et al. (2016) Copyright 2016 Royal Society of Chemistry.

(D) Calculated free energy diagram of CO_2 reduction to CO. Reprinted with permission from Pan et al. (2018) Copyright 2018 American Chemical Society.

(E) CO Faradaic efficiency of Fe-SAC at different potentials. Reprinted with permission from Pan et al. (2018) Copyright 2018 American Chemical Society.

(F) Schematic of the synthetic process of Re-SAC. Reprinted with permission from Ye et al. (2016) Copyright 2016 Royal Society of Chemistry.

(G and H) Faradaic efficiency for different reduction products at different potentials of Mn-NC (G) and Mn-SNC (H) showing Mn-SNC with better selectivity to CO. Reprinted with permission from Tan et al. (2021) Copyright 2021 American Chemical Society.

(I) Schematic of the structure of the intermediate *COOH absorbed on the single atom. Reprinted with permission from Tan et al. (2021) Copyright 2021 American Chemical Society.

both transition metals and post-transition metals. Transition metals tend to combine with carbon atoms, whereas post-transition metals tend to interact with oxygen atom to form chemical bonds (Birdja et al., 2019; Wang et al., 2020b). Different bonding ways would affect the subsequent reaction of reactive intermediates (Zhu et al., 2021). However, the current research on post transition metal catalysts is insufficient, which may exhibit different catalytic behaviors.

In addition, the formation of the C-C bond results in reduction product containing more than two carbon atoms, which has higher economic value than carbon monoxide. However, the formation of C-C bonds often involves the interaction of more than two active intermediates (Zhao et al., 2020b). For SACs, the active sites are relatively dispersed, and it is relatively difficult to produce reduction products above C_2.

CONCLUSION AND PERSPECTIVE

MOF-based and MOF-derived materials provide a wealth of strategies for the preparation of SACs. Researchers could use their creativity and imagination to construct MOF-based and MOF-derived SACs with different structures and properties. The combination of the highly efficient active site of SACs with

Table 2. Representative examples of SACs with MOFs as precursors for electrocatalytic CO_2RR

Catalyst	Precursor	Synthesis strategy	Main product	Electrolyte	pH	Faradaic efficiency	Potential	Current density	Reactor	Reference
Bi-NC	Bi-BTC	Derivate capture	CO	0.1 M $NaHCO_3$	7	>97%	−0.50 V	5.1 mA cm^{-2}	H-cell	(Zhang et al., 2019)
Co-N_4	ZIF-8	Node stabilization	CO	0.1 M $KHCO_3$	6.8	82%	−1.1 V	18 mA cm^{-2}	H-cell	(Geng et al., 2019)
Co-NC	PCN-222	Ligand stabilization	CO	0.1 M $KHCO_3$	6.8	98.7%	−0.6 V	~3 mA cm^{-2}	H-cell	(Zhou et al., 2021a)
Cu-NC	Cu-BTC	Node stabilization	CH_4	0.1 M $KHCO_3$	6.8	38.6%	−1.6 V	14.8 mA cm^{-2}	H-cell	(Guan et al., 2020)
Cu-NC	ZIF-8	Node stabilization	C_2H_5OH	0.1 M $CsHCO_3$	6.8	55%	−1.2 V	NA	H-cell	(Karapinar et al., 2019)
Cu-N_4	ZIF-8	Node stabilization	CO	0.5 M $KHCO_3$	NA	93%	−0.67 V	6.7 mA cm^{-2}	Flow cell	(Cheng et al., 2021)
Cu-NC	ZIF-8	Composite	CH_3OH/CO	0.1 M $KHCO_3$	NA	44%/56%	−0.9 V	93 mA cm^{-2}	H-cell	(Yang et al., 2019)
Cu-NC	ZIF-8	Node stabilization	CH_3COCH_3	0.1 M $KHCO_3$	NA	36.7%	−0.36 V	~12 mA cm^{-2}	double-cell	(Zhao et al., 2020a)
Fe-NC	ZIF-8	Node stabilization	CO	0.5 M $KHCO_3$	7.3	86.9%	−0.47 V	2.90 mA cm^{-2}	H-cell	(Chen et al., 2020b)
Fe-NC	ZIF-8	Node stabilization	CO	0.5 M $KHCO_3$	NA	93%	−0.4 V	4 mA cm^{-2}	H-cell	(Li et al., 2021)
Fe-NC	ZIF-8	Derivate capture	CO	0.1 M $KHCO_3$	NA	>90%	−0.8 V	25 mA cm^{-2}	H-cell	(Mohd Adli et al., 2021)
Fe-NC	ZIF-7	Ligand stabilization	CO	1.0 M $KHCO_3$	7.8	>80%	−0.43 V	17.8 mA cm^{-2}	H-cell	(Yan et al., 2019)
CoPc@Fe-NC	ZIF-8	Node stabilization	CO	0.5 M KOH	13.7	>90%	−0.84 V	275.6 ± 27.0 mA cm^{-2}	Flow cell	(Lin et al., 2019)
In-NC	ZIF-8	Node stabilization	HCOOH	0.5 M $KHCO_3$	7.2	NA	−0.99 V	NA	H-cell	(Lu et al., 2021)
In-NC	ZIF-8	Pore confinement	HCOOH	0.5 M $KHCO_3$	NA	96%	−0.65 V	8.87 mA cm^{-2}	H-cell	(Shang et al., 2020)
Mn-SNC	ZIF-8	Node stabilization	CO	0.5 M $KHCO_3$	NA	70%	−0.45 V	NA	NA	(Tan et al., 2021)
Ni-NC	ZIF-8	Node stabilization	CO	0.5 M $KHCO_3$	7.2	97%	−0.9 V	41.5 mA cm^{-2}	double-cell	(Lu et al., 2019)
Ni-NC	ZIF-8	Node stabilization	CO	0.5 M $KHCO_3$	7.2	95.1%	NA	10.2 mA cm^{-2}	double-cell	(Ma et al., 2019)
Ni-NC	Ni-BDC	Node stabilization	CO	0.5 M $KHCO_3$	7.2	97%	−0.9 V	27.2 mA cm^{-2}	H-cell	(Wang et al., 2021b)
Ni-N_4O	Mn-BDC	Node stabilization	CO	0.5 M $KHCO_3$	7.3	99.2%	−0.9 V	23 mA cm^{-2}	H-cell	(Wang et al., 2021c)
Ni/Fe-NC	ZIF-8	Node stabilization	CO	0.5 M $KHCO_3$	NA	98%	−0.7 V	7.4 mA cm^{-2}	H-cell	(Ren et al., 2019)
Ni–N_4/C–NH_2	ZIF-8	Node stabilization	CO	0.5 M $KHCO_3$	7.33	96.2%	−0.8 V	63.6 mA cm^{-2}	H-cell	(Chen et al., 2021c)
Ni-NC	ZIF-8	Node stabilization	CO	0.5 M $KHCO_3$	NA	98%	−1.0 V	34.3 mA cm^{-2}	double-cell	(Hou et al., 2020b)
Ni-NC	Ni-PCN	Node stabilization	CO	0.5 M $KHCO_3$	7.2	96.8%	−0.8 V	27 mA cm^{-2}	H-cell	(Jiao et al., 2020)
Ni-N_2-C	MOF-74	Node stabilization	CO	0.5 M $KHCO_3$	7.2	98%	−0.8 V	~10 mA cm^{-2}	H-cell	(Gong et al., 2020)
Ni-NC	Ni_2(NDISA)	Composite	CO	0.5 M $KHCO_3$	NA	96%	−0.67 V	NA	H-cell	(Yang et al., 2020)
ZIF-A-LD/CB	ZIF-8	Node stabilization	CO	0.1 M $KHCO_3$	6.8	90.57%	−1.1 V	6.83 mA cm^{-2}	H-cell	(Dou et al., 2019)

CellPress
OPEN ACCESS

the excellent mass transfer and photoelectric properties of MOFs makes the MOF-based and MOF-derived SACs perform excellently in the photoelectric CO_2RR. Except serving as supports of SACs, it is easier for MOFs to introduce other functional units into the system, including photoactive groups or structural units with special properties for gas adsorption. MOFs are good tools for integrating required functions. With the special active center structure and excellent catalytic performance of SACs, it is expected to prepare non-noble metal catalysts for CO_2RR in addition to traditional gold-/silver-based catalysts. Coupled with the special adsorption properties of MOFs for gas molecules, CO_2 as a reactant could be captured by MOFs and enriched near the active sites.

Based on the current exploration of the application of MOF-based SACs, the following problems still exist:

- poor economic benefits of products;
- environmental problems brought by photosensitizers;
- insufficient durability.

The current research on carbon dioxide reduction is still mainly limited to relatively simple reduction products containing only one carbon atom. The photosensitizers and sacrificial agents used in photocatalysis are not environmentally friendly, which hinders practical applications. Besides, MOFs have limited resistance to chemical environments. It is more suitable for application under relatively mild conditions. Although heat treatment could improve stability, it also means that organic components would be carbonized and lose their special properties. How to achieve efficient and highly selective reduction to obtain products with more economic value is still a problem to be solved. Here are a few ideas to consider:

- high loading SACs;
- dual or multiple atom site catalysts;
- modulation of selectivity by pores of MOFs.

The reduction process containing multiple carbon atoms often involves the coupling of multiple catalytic active centers and active intermediates. This requires that the active sites have a considerable density and are relatively close in space, so that the active intermediates can meet and combine well. This poses a challenge for the preparation of SACs. How to enhance the metal loading while ensuring the dispersion of single atom still requires more research and attempts. The coupling of different catalytic active sites is also an important issue. The abundant strategies of the preparation for SACs enable different metal elements to be introduced to synthesize single-atom alloy catalysts. Thus, new materials with different catalytic properties could be obtained. Various pathways are involved in CO_2RR. The matching relationship between products and pores influences the selectivity, which is also worth exploring. The special adsorption behavior of MOFs for products is related to the selectivity of the reactions. So, SACs prepared with MOFs as precursors might show unusual catalytic selectivity. MOFs are still good platforms for the construction of SACs, which could provide ideas for the construction of carbon dioxide reduction catalysts.

ACKNOWLEDGMENTS

This work was supported by the National Key R&D Program of China (2018YFA0702003), the National Natural Science Foundation of China (21890383, 22102119, 21871159, and 52002249), the Guangdong Basic and Applied Basic Research Foundation (2019A1515110025), and the Science and Technology Key Project of Guangdong Province of China (2020B010188002). We thank Professor Fang Yang from Tsinghua University for assistance on polishing the manuscript.

AUTHOR CONTRIBUTIONS

Writing – original Draft, X.L.; writing – review and editing, S.J., Y.C., and D.W.; funding acquisition – D.W.; supervision – S.J. and D.W.

DECLARATION OF INTERESTS

The authors declare no conflict of interest.

CellPress
OPEN ACCESS

REFERENCES

Abdel-Mageed, A.M., Rungtaweevoranit, B., Parlinska-Wojtan, M., Pei, X., Yaghi, O.M., and Behm, R.J. (2019). Highly active and stable single-atom Cu catalysts supported by a metal-organic framework. J. Am. Chem. Soc. *141*, 5201–5210. https://doi.org/10.1021/jacs.8b11386.

Angulo-Ibanez, A., Goitandia, A.M., Albo, J., Aranzabe, E., Beobide, G., Castillo, O., and Perez-Yanez, S. (2021). Porous TiO_2 thin film-based photocatalytic windows for an enhanced operation of optofluidic microreactors in CO_2 conversion. iScience *24*, 102654. https://doi.org/10.1016/j.isci.2021.102654.

Birdja, Y.Y., Pérez-Gallent, E., Figueiredo, M.C., Göttle, A.J., Calle-Vallejo, F., and Koper, M.T.M. (2019). Advances and challenges in understanding the electrocatalytic conversion of carbon dioxide to fuels. Nat. Energy *4*, 732–745. https://doi.org/10.1038/s41560-019-0450-y.

Chen, S., Li, W.H., Jiang, W., Yang, J., Zhu, J., Wang, L., Ou, H., Zhuang, Z., Chen, M., Sun, X., et al. (2022). MOF encapsulating N-Heterocyclic carbene-ligated copper single-atom site catalyst towards efficient methane electrosynthesis. Angew. Chem. Int. Ed. *61*, e202114450. https://doi.org/10.1002/anie.202114450.

Chen, W., Pei, J., He, C.T., Wan, J., Ren, H., Wang, Y., Dong, J., Wu, K., Cheong, W.C., Mao, J., et al. (2018). Single tungsten atoms supported on MOF-derived N-doped carbon for robust electrochemical hydrogen evolution. Adv. Mater. *30*, e1800396. https://doi.org/10.1002/adma.201800396.

Chen, X.-H., Wei, Q., Hong, J.-D., Xu, R., and Zhou, T.-H. (2019). Bifunctional metal–organic frameworks toward photocatalytic CO_2 reduction by post-synthetic ligand exchange. Rare Met. *38*, 413–419. https://doi.org/10.1007/s12598-019-01259-6.

Chen, S., Su, Y., Deng, P., Qi, R., Zhu, J., Chen, J., Wang, Z., Zhou, L., Guo, X., and Xia, B.Y. (2020a). Highly selective carbon dioxide electroreduction on structure-evolved copper perovskite oxide toward methane production. ACS Catal. *10*, 4640–4646. https://doi.org/10.1021/acscatal.0c00847.

Chen, X., Ma, D.-D., Chen, B., Zhang, K., Zou, R., Wu, X.-T., and Zhu, Q.-L. (2020b). Metal–organic framework-derived mesoporous carbon nanoframes embedded with atomically dispersed Fe–N active sites for efficient bifunctional oxygen and carbon dioxide electroreduction. Appl. Catal. B *267*, 118720. https://doi.org/10.1016/j.apcatb.2020.118720.

Chen, S., Wang, B., Zhu, J., Wang, L., Ou, H., Zhang, Z., Liang, X., Zheng, L., Zhou, L., Su, Y.Q., et al. (2021a). Lewis acid site-promoted single-atomic Cu Catalyzes electrochemical CO_2 methanation. Nano Lett. *21*, 7325–7331. https://doi.org/10.1021/acs.nanolett.1c02502.

Chen, Y., Gao, R., Ji, S., Li, H., Tang, K., Jiang, P., Hu, H., Zhang, Z., Hao, H., Qu, Q., et al. (2021b). Atomic-level modulation of electronic density at cobalt single-atom sites derived from metal-organic frameworks: enhanced oxygen reduction performance. Angew. Chem. Int. Ed. *60*, 3212–3221. https://doi.org/10.1002/anie.202012798.

Chen, Z., Zhang, X., Liu, W., Jiao, M., Mou, K., Zhang, X., and Liu, L. (2021c). Amination strategy to boost the CO_2 electroreduction current density of M–N/C single-atom catalysts to the industrial application level. Energy Environ. Sci. *14*, 2349–2356. https://doi.org/10.1039/d0ee04052e.

Cheng, H., Wu, X., Li, X., Nie, X., Fan, S., Feng, M., Fan, Z., Tan, M., Chen, Y., and He, G. (2021). Construction of atomically dispersed Cu-N_4 sites via engineered coordination environment for high-efficient CO_2 electroreduction. Chem. Eng. J. *407*, 126842. https://doi.org/10.1016/j.cej.2020.126842.

Cheng, N., Zhang, L., Doyle-Davis, K., and Sun, X. (2019). Single-atom catalysts: from design to application. Electrochem. Energy Rev. *2*, 539–573. https://doi.org/10.1007/s41918-019-00050-6.

Choi, K.M., Kim, D., Rungtaweevoranit, B., Trickett, C.A., Barmanbek, J.T., Alshammari, A.S., Yang, P., and Yaghi, O.M. (2017). Plasmon-Enhanced photocatalytic CO_2 conversion within metal-organic frameworks under visible light. J. Am. Chem. Soc. *139*, 356–362. https://doi.org/10.1021/jacs.6b11027.

Choi, S., Jung, W.J., Park, K., Kim, S.Y., Baeg, J.O., Kim, C.H., Son, H.J., Pac, C., and Kang, S.O. (2021). Rapid exciton migration and amplified funneling effects of multi-porphyrin arrays in a Re(I)/Porphyrinic MOF hybrid for photocatalytic CO_2 reduction. ACS Appl. Mater. Inter. *13*, 2710–2722. https://doi.org/10.1021/acsami.0c19856.

Chu, S., Ou, P., Rashid, R.T., Ghamari, P., Wang, R., Tran, H.N., Zhao, S., Zhang, H., Song, J., and Mi, Z. (2020). Decoupling strategy for enhanced syngas generation from photoelectrochemical CO_2 reduction. iScience *23*, 101390. https://doi.org/10.1016/j.isci.2020.101390.

Cui, T., Wang, Y.P., Ye, T., Wu, J., Chen, Z., Li, J., Lei, Y., Wang, D., and Li, Y. (2022). Engineering dual single-atom sites on 2D ultrathin N-doped carbon nanosheets attaining ultra-low temperature Zn-air battery. Angew. Chem. Int. Ed. https://doi.org/10.1002/anie.202115219.

Deng, P., Wang, H., Qi, R., Zhu, J., Chen, S., Yang, F., Zhou, L., Qi, K., Liu, H., and Xia, B.Y. (2019). Bismuth oxides with enhanced bismuth–oxygen structure for efficient electrochemical reduction of carbon dioxide to formate. ACS Catal. *10*, 743–750. https://doi.org/10.1021/acscatal.9b04043.

Dou, S., Song, J., Xi, S., Du, Y., Wang, J., Huang, Z.F., Xu, Z.J., and Wang, X. (2019). Boosting electrochemical CO_2 reduction on metal-organic frameworks via ligand doping. Angew. Chem. Int. Ed. *58*, 4041–4045. https://doi.org/10.1002/anie.201814711.

Fei, H., Sampson, M.D., Lee, Y., Kubiak, C.P., and Cohen, S.M. (2015). Photocatalytic CO2 reduction to formate using a Mn(I) molecular catalyst in a robust metal-organic framework. Inorg. Chem. *54*, 6821–6828. https://doi.org/10.1021/acs.inorgchem.5b00752.

Feng, X., Pan, F., Zhang, P., Wang, X., Zhou, H.C., Huang, Y., and Li, Y. (2020). Metal-organic framework MIL-125 derived Mg^{2+}-doped mesoporous TiO_2 for photocatalytic CO_2 reduction. ChemPhotoChem *5*, 79–89. https://doi.org/10.1002/cptc.202000181.

Gao, J., Hu, Y., Wang, Y., Lin, X., Hu, K., Lin, X., Xie, G., Liu, X., Reddy, K.M., Yuan, Q., and Qiu, H.J. (2021). MOF structure engineering to synthesize CoNC catalyst with richer accessible active sites for enhanced oxygen reduction. Small *17*, e2104684. https://doi.org/10.1002/smll.202104684.

Geng, W., Chen, W., Li, G., Dong, X., Song, Y., Wei, W., and Sun, Y. (2020). Induced CO_2 electroreduction to formic acid on metal-organic frameworks via node doping. ChemSusChem *13*, 4035–4040. https://doi.org/10.1002/cssc.202001310.

Geng, Z., Cao, Y., Chen, W., Kong, X., Liu, Y., Yao, T., and Lin, Y. (2019). Regulating the coordination environment of Co single atoms for achieving efficient electrocatalytic activity in CO_2 reduction. Appl. Catal. B *240*, 234–240. https://doi.org/10.1016/j.apcatb.2018.08.075.

Gong, Y.N., Jiao, L., Qian, Y., Pan, C.Y., Zheng, L., Cai, X., Liu, B., Yu, S.H., and Jiang, H.L. (2020). Regulating the coordination environment of MOF-templated single-atom nickel electrocatalysts for boosting CO_2 reduction. Angew. Chem. Int. Ed. *59*, 2705–2709. https://doi.org/10.1002/anie.201914977.

Guan, A., Chen, Z., Quan, Y., Peng, C., Wang, Z., Sham, T.-K., Yang, C., Ji, Y., Qian, L., Xu, X., and Zheng, G. (2020). Boosting CO_2 electroreduction to CH_4 via tuning neighboring single-copper sites. ACS Energy Lett *5*, 1044–1053. https://doi.org/10.1021/acsenergylett.0c00018.

Guan, X., Mao, S.S., and Shen, S. (2021). Recent progress on photocatalytic CO_2 reduction with eart-abundant single-atom reactive sites. ChemNanoMat *7*, 873–880. https://doi.org/10.1002/cnma.202100103.

Guo, Y., Feng, L., Wu, C., Wang, X., and Zhang, X. (2020). Confined pyrolysis transformation of ZIF-8 to hierarchically ordered porous Zn-N-C nanoreactor for efficient CO_2 photoconversion under mild conditions. J. Catal. *390*, 213–223. https://doi.org/10.1016/j.jcat.2020.07.037.

Han, A., Wang, X., Tang, K., Zhang, Z., Ye, C., Kong, K., Hu, H., Zheng, L., Jiang, P., Zhao, C., et al. (2021). An adjacent atomic platinum site enables single-atom iron with high oxygen reduction reaction performance. Angew. Chem. Int. Ed. *60*, 19262–19271. https://doi.org/10.1002/anie.202105186.

Handoko, A.D., Chen, H., Lum, Y., Zhang, Q., Anasori, B., and Seh, Z.W. (2020). Two-dimensional titanium and molybdenum carbide MXenes as electrocatalysts for CO_2 reduction. iScience *23*, 101181. https://doi.org/10.1016/j.isci.2020.101181.

Hao, Y.C., Chen, L.W., Li, J., Guo, Y., Su, X., Shu, M., Zhang, Q., Gao, W.Y., Li, S., Yu, Z.L., et al. (2021). Metal-organic framework membranes with single-atomic centers for photocatalytic CO_2 and O_2 reduction. Nat. Commun. *12*, 2682. https://doi.org/10.1038/s41467-021-22991-7.

He, Q., Liu, D., Lee, J.H., Liu, Y., Xie, Z., Hwang, S., Kattel, S., Song, L., and Chen, J.G. (2020).

Electrochemical conversion of CO_2 to syngas with controllable CO/H_2 ratios over Co and Ni single-atom catalysts. Angew. Chem. Int. Ed. *59*, 3033–3037. https://doi.org/10.1002/anie.201912719.

Hou, C.-C., Wang, H.-F., Li, C., and Xu, Q. (2020a). From metal–organic frameworks to single/dual-atom and cluster metal catalysts for energy applications. Energy Environ. Sci. *13*, 1658–1693. https://doi.org/10.1039/c9ee04040d.

Hou, Y., Liang, Y.-L., Shi, P.-C., Huang, Y.-B., and Cao, R. (2020b). Atomically dispersed Ni species on N-doped carbon nanotubes for electroreduction of CO_2 with nearly 100% CO selectivity. Appl. Catal. B *271*, 118929. https://doi.org/10.1016/j.apcatb.2020.118929.

Hu, L., Deng, B., Du, K., Jiang, R., Dou, Y., and Wang, D. (2020). Tunable selectivity and high efficiency of CO_2 electroreduction via borate-enhanced molten salt electrolysis. iScience *23*, 101607. https://doi.org/10.1016/j.isci.2020.101607.

Huang, H., Shen, K., Chen, F., and Li, Y. (2020). Metal–organic frameworks as a good platform for the fabrication of single-atom catalysts. ACS Catal. *10*, 6579–6586. https://doi.org/10.1021/acscatal.0c01459.

Huang, R., Peng, Y., Wang, C., Shi, Z., and Lin, W. (2016). A rhenium-functionalized metal–organic framework as a single-site catalyst for photochemical reduction of carbon dioxide. Eur. J. Inorg. Chem. *2016*, 4358–4362. https://doi.org/10.1002/ejic.201600064.

Ikreedeegh, R.R., and Tahir, M. (2021). A critical review in recent developments of metal-organic-frameworks (MOFs) with band engineering alteration for photocatalytic CO_2 reduction to solar fuels. J. CO2 Util. *43*, 101381. https://doi.org/10.1016/j.jcou.2020.101381.

Jiao, L., and Jiang, H.-L. (2019). Metal-organic-framework-based single-atom catalysts for energy applications. Chem *5*, 786–804. https://doi.org/10.1016/j.chempr.2018.12.011.

Jiao, L., Yang, W., Wan, G., Zhang, R., Zheng, X., Zhou, H., Yu, S.H., and Jiang, H.L. (2020). Single-atom electrocatalysts from multivariate metal-organic frameworks for highly selective reduction of CO_2 at low pressures. Angew. Chem. Int. Ed. *59*, 20589–20595. https://doi.org/10.1002/anie.202008787.

Jing, H., Zhu, P., Zheng, X., Zhang, Z., Wang, D., and Li, Y. (2021). Theory-oriented screening and discovery of advanced energy transformation materials in electrocatalysis. Adv. Powder Mater. https://doi.org/10.1016/j.apmate.2021.10.004.

Kajiwara, T., Fujii, M., Tsujimoto, M., Kobayashi, K., Higuchi, M., Tanaka, K., and Kitagawa, S. (2016). Photochemical reduction of low concentrations of CO_2 in a porous coordination polymer with a ruthenium(II)-CO complex. Angew. Chem. Int. Ed. *55*, 2697–2700. https://doi.org/10.1002/anie.201508941.

Karapinar, D., Huan, N.T., Ranjbar Sahraie, N., Li, J., Wakerley, D., Touati, N., Zanna, S., Taverna, D., Galvao Tizei, L.H., Zitolo, A., et al. (2019). Electroreduction of CO_2 on single-site copper-nitrogen-doped carbon material: selective formation of ethanol and reversible restructuration of the metal sites. Angew. Chem. Int. Ed. *58*, 15098–15103. https://doi.org/10.1002/anie.201907994.

Kim, J., Choi, W., Park, J.W., Kim, C., Kim, M., and Song, H. (2019). Branched copper oxide nanoparticles induce highly selective ethylene production by electrochemical carbon dioxide reduction. J. Am. Chem. Soc. *141*, 6986–6994. https://doi.org/10.1021/jacs.9b00911.

Lee, Y., Kim, S., Fei, H., Kang, J.K., and Cohen, S.M. (2015). Photocatalytic CO_2 reduction using visible light by metal-monocatecholato species in a metal-organic framework. Chem. Commun. *51*, 16549–16552. https://doi.org/10.1039/c5cc04506a.

Li, M., Wang, H., Luo, W., Sherrell, P.C., Chen, J., and Yang, J. (2020a). Heterogeneous single-atom catalysts for electrochemical CO_2 reduction reaction. Adv. Mater. *32*, e2001848. https://doi.org/10.1002/adma.202001848.

Li, X., Rong, H., Zhang, J., Wang, D., and Li, Y. (2020b). Modulating the local coordination environment of single-atom catalysts for enhanced catalytic performance. Nano Res. *13*, 1842–1855. https://doi.org/10.1007/s12274-020-2755-3.

Li, X., Zeng, Y., Tung, C.-W., Lu, Y.-R., Baskaran, S., Hung, S.-F., Wang, S., Xu, C.-Q., Wang, J., Chan, T.-S., et al. (2021). Unveiling the *in situ* generation of a monovalent Fe(I) site in the single-Fe-atom catalyst for electrochemical CO_2 reduction. ACS Catal. *11*, 7292–7301. https://doi.org/10.1021/acscatal.1c01621.

Li, Y., Wang, S., Wang, X.S., He, Y., Wang, Q., Li, Y., Li, M., Yang, G., Yi, J., Lin, H., et al. (2020c). Facile top-down strategy for direct metal atomization and coordination achieving a high turnover number in CO_2 photoreduction. J. Am. Chem. Soc. *142*, 19259–19267. https://doi.org/10.1021/jacs.0c09060.

Lin, L., Li, H., Yan, C., Li, H., Si, R., Li, M., Xiao, J., Wang, G., and Bao, X. (2019). Synergistic catalysis over iron-nitrogen sites anchored with cobalt phthalocyanine for efficient CO_2 electroreduction. Adv. Mater. *31*, e1903470. https://doi.org/10.1002/adma.201903470.

Liu, M., Mu, Y.-F., Yao, S., Guo, S., Guo, X.-W., Zhang, Z.-M., and Lu, T.-B. (2019). Photosensitizing single-site metal-organic framework enabling visible-light-driven CO_2 reduction for syngas production. Appl. Catal. B *245*, 496–501. https://doi.org/10.1016/j.apcatb.2019.01.014.

Lu, P., Tan, X., Zhao, H., Xiang, Q., Liu, K., Zhao, X., Yin, X., Li, X., Hai, X., Xi, S., et al. (2021). Atomically dispersed indium sites for selective CO_2 electroreduction to formic acid. ACS Nano *15*, 5671–5678. https://doi.org/10.1021/acsnano.1c00858.

Lu, P., Yang, Y., Yao, J., Wang, M., Dipazir, S., Yuan, M., Zhang, J., Wang, X., Xie, Z., and Zhang, G. (2019). Facile synthesis of single-nickel-atomic dispersed N-doped carbon framework for efficient electrochemical CO_2 reduction. Appl. Catal. B *241*, 113–119. https://doi.org/10.1016/j.apcatb.2018.09.025.

Luo, Y.-H., Dong, L.-Z., Liu, J., Li, S.-L., and Lan, Y.-Q. (2019). From molecular metal complex to metal-organic framework: the CO_2 reduction photocatalysts with clear and tunable structure. Coord. Chem. Rev. *390*, 86–126. https://doi.org/10.1016/j.ccr.2019.03.019.

Ma, Z., Wu, D., Han, X., Wang, H., Zhang, L., Gao, Z., Xu, F., and Jiang, K. (2019). Ultrasonic assisted synthesis of Zn-Ni bi-metal MOFs for interconnected Ni-N-C materials with enhanced electrochemical reduction of CO_2. J. CO2 Util. *32*, 251–258. https://doi.org/10.1016/j.jcou.2019.04.006.

Mohd Adli, N., Shan, W., Hwang, S., Samarakoon, W., Karakalos, S., Li, Y., Cullen, D.A., Su, D., Feng, Z., Wang, G., and Wu, G. (2021). Engineering atomically dispersed FeN4 active sites for CO_2 electroreduction. Angew. Chem. Int. Ed. *60*, 1022–1032. https://doi.org/10.1002/anie.202012329.

Pan, F., Zhang, H., Liu, K., Cullen, D., More, K., Wang, M., Feng, Z., Wang, G., Wu, G., and Li, Y. (2018). Unveiling active sites of CO_2 reduction on nitrogen-coordinated and atomically dispersed iron and cobalt catalysts. ACS Catal. *8*, 3116–3122. https://doi.org/10.1021/acscatal.8b00398.

Peng, Y., Lu, B., and Chen, S. (2018). Carbon-supported single atom catalysts for electrochemical energy conversion and storage. Adv. Mater. *30*, e1801995. https://doi.org/10.1002/adma.201801995.

Quan, Y., Zhu, J., and Zheng, G. (2021). Electrocatalytic reactions for converting CO_2 to value-added products. Small Sci. *1*, 2100043. https://doi.org/10.1002/smsc.202100043.

Ren, W., Tan, X., Yang, W., Jia, C., Xu, S., Wang, K., Smith, S.C., and Zhao, C. (2019). Isolated diatomic Ni-Fe metal-nitrogen sites for synergistic electroreduction of CO_2. Angew. Chem. Int. Ed. *58*, 6972–6976. https://doi.org/10.1002/anie.201901575.

Shah, S.S.A., Najam, T., Wen, M., Zang, S.-Q., Waseem, A., and Jiang, H.-L. (2021). Metal–organic framework-based electrocatalysts for CO_2 reduction. Small Struct. 2100090. https://doi.org/10.1002/sstr.202100090.

Shang, H., Wang, T., Pei, J., Jiang, Z., Zhou, D., Wang, Y., Li, H., Dong, J., Zhuang, Z., Chen, W., et al. (2020). Design of a single-atom indium(delta+) -N4 interface for efficient electroreduction of CO_2 to formate. Angew. Chem. Int. Ed. *59*, 22465–22469. https://doi.org/10.1002/anie.202010903.

Sun, D., Gao, Y., Fu, J., Zeng, X., Chen, Z., and Li, Z. (2015). Construction of a supported Ru complex on bifunctional MOF-253 for photocatalytic CO_2 reduction under visible light. Chem. Commun. *51*, 2645–2648. https://doi.org/10.1039/c4cc09797a.

Sun, T., Xu, L., Wang, D., and Li, Y. (2019). Metal organic frameworks derived single atom catalysts for electrocatalytic energy conversion. Nano Res. *12*, 2067–2080. https://doi.org/10.1007/s12274-019-2345-4.

Sun, X., Tuo, Y., Ye, C., Chen, C., Lu, Q., Li, G., Jiang, P., Chen, S., Zhu, P., Ma, M., et al. (2021). Phosphorus induced electron localization of single iron sites for boosted CO_2 electroreduction reaction. Angew. Chem. Int. Ed. *60*, 23614–23618. https://doi.org/10.1002/anie.202110433.

Tan, H.Y., Lin, S.C., Wang, J., Chang, C.J., Haw, S.C., Lin, K.H., Tsai, L.D., Chen, H.C., and Chen, H.M. (2021). MOF-templated sulfurization of atomically dispersed manganese catalysts facilitating electroreduction of CO_2 to CO. ACS Appl. Mater. Inter. *13*, 52134–52143. https://doi.org/10.1021/acsami.1c10059.

Ting, L.R.L., Garcia-Muelas, R., Martin, A.J., Veenstra, F.L.P., Chen, S.T., Peng, Y., Per, E.Y.X., Pablo-Garcia, S., Lopez, N., Perez-Ramirez, J., and Yeo, B.S. (2020). Electrochemical reduction of carbon dioxide to 1-butanol on oxide-derived copper. Angew. Chem. Int. Ed. *59*, 21072–21079. https://doi.org/10.1002/anie.202008289.

Wang, G., He, C.T., Huang, R., Mao, J., Wang, D., and Li, Y. (2020a). Photoinduction of Cu single atoms decorated on UiO-66-NH_2 for enhanced photocatalytic reduction of CO_2 to liquid fuels. J. Am. Chem. Soc. *142*, 19339–19345. https://doi.org/10.1021/jacs.0c09599.

Wang, J., Guan, Y., Yu, X., Cao, Y., Chen, J., Wang, Y., Hu, B., and Jing, H. (2020b). Photoelectrocatalytic reduction of CO_2 to paraffin using p-n heterojunctions. iScience *23*, 100768. https://doi.org/10.1016/j.isci.2019.100768.

Wang, Z., Akter Monny, S., and Wang, L. (2020c). Hollow structure for photocatalytic CO_2 reduction. ChemNanoMat *6*, 881–888. https://doi.org/10.1002/cnma.202000157.

Wang, F., Qian, G., Kong, X.P., Zhao, X., Hou, T., Chen, L., Fang, R., and Li, Y. (2021a). Hierarchical double-shelled CoP nanocages for efficient visible-light-driven CO_2 reduction. ACS Appl. Mater. Inter. *13*, 45609–45618. https://doi.org/10.1021/acsami.1c13881.

Wang, H., Liu, G., Chen, C., Tu, W., Lu, Y., Wu, S., O'Hare, D., and Xu, R. (2021b). Single-Ni sites embedded in multilayer nitrogen-doped graphene derived from amino-functionalized MOF for highly selective CO_2 electroreduction. ACS Sustainable Chem. Eng. *9*, 3792–3801. https://doi.org/10.1021/acssuschemeng.0c08749.

Wang, X., Wang, Y., Sang, X., Zheng, W., Zhang, S., Shuai, L., Yang, B., Li, Z., Chen, J., Lei, L., et al. (2021c). Dynamic activation of adsorbed intermediates via axial traction for the promoted electrochemical CO_2 reduction. Angew. Chem. Int. Ed. *60*, 4192–4198. https://doi.org/10.1002/anie.202013427.

Wang, Y., Zheng, X., and Wang, D. (2021d). Design concept for electrocatalysts. Nano Res. 1–23. https://doi.org/10.1007/s12274-021-3794-0.

Wang, Y., Zheng, M., Li, Y., Ye, C., Chen, J., Ye, J., Zhang, Q., Li, J., Zhou, Z., Fu, X.Z., et al. (2022). P-d orbital hybridization induced by monodispersed Ga site on Pt_3Mn nanocatalyst boosts ethanol electrooxidation. Angew. Chem. Int. Ed. https://doi.org/10.1002/anie.202115735.

Wen, C.F., Mao, F., Liu, Y., Zhang, X.Y., Fu, H.Q., Zheng, L.R., Liu, P.F., and Yang, H.G. (2019). Nitrogen-stabilized low-valent Ni motifs for efficient CO_2 electrocatalysis. ACS Catal. *10*, 1086–1093. https://doi.org/10.1021/acscatal.9b02978.

Xiong, Y., Sun, W., Han, Y., Xin, P., Zheng, X., Yan, W., Dong, J., Zhang, J., Wang, D., and Li, Y. (2021). Cobalt single atom site catalysts with ultrahigh metal loading for enhanced aerobic oxidation of ethylbenzene. Nano Res. *14*, 2418–2423. https://doi.org/10.1007/s12274-020-3244-4.

Yan, C., Ye, Y., Lin, L., Wu, H., Jiang, Q., Wang, G., and Bao, X. (2019). Improving CO_2 electroreduction over ZIF-derived carbon doped with Fe-N sites by an additional ammonia treatment. Catal. Today *330*, 252–258. https://doi.org/10.1016/j.cattod.2018.03.062.

Yang, F., Song, P., Liu, X., Mei, B., Xing, W., Jiang, Z., Gu, L., and Xu, W. (2018a). Highly efficient CO_2 electroreduction on ZnN_4-based single-atom catalyst. Angew. Chem. Int. Ed. *57*, 12303–12307. https://doi.org/10.1002/anie.201805871.

Yang, J., Qiu, Z., Zhao, C., Wei, W., Chen, W., Li, Z., Qu, Y., Dong, J., Luo, J., Li, Z., and Wu, Y. (2018b). *In situ* thermal atomization to convert supported nickel nanoparticles into surface-bound nickel single-atom catalysts. Angew. Chem. Int. Ed. *57*, 14095–14100. https://doi.org/10.1002/anie.201808049.

Yang, H., Wu, Y., Li, G., Lin, Q., Hu, Q., Zhang, Q., Liu, J., and He, C. (2019). Scalable production of efficient single-atom copper decorated carbon membranes for CO_2 electroreduction to methanol. J. Am. Chem. Soc. *141*, 12717–12723. https://doi.org/10.1021/jacs.9b04907.

Yang, J., Li, W.H., Tan, S., Xu, K., Wang, Y., Wang, D., and Li, Y. (2021). The electronic metal-support interaction directing the design of single atomic site catalysts: achieving high efficiency towards hydrogen evolution. Angew. Chem. Int. Ed. *60*, 19085–19091. https://doi.org/10.1002/anie.202107123.

Yang, S., Zhang, J., Peng, L., Asgari, M., Stoian, D., Kochetygov, I., Luo, W., Oveisi, E., Trukhina, O., Clark, A.H., et al. (2020). A metal-organic framework/polymer derived catalyst containing single-atom nickel species for electrocatalysis. Chem. Sci. *11*, 10991–10997. https://doi.org/10.1039/d0sc04512h.

Ye, L., Liu, J., Gao, Y., Gong, C., Addicoat, M., Heine, T., Wöll, C., and Sun, L. (2016). Highly oriented MOF thin film-based electrocatalytic device for the reduction of CO_2 to CO exhibiting high faradaic efficiency. J. Mater. Chem. A. *4*, 15320–15326. https://doi.org/10.1039/c6ta04801c.

Zhang, E., Wang, T., Yu, K., Liu, J., Chen, W., Li, A., Rong, H., Lin, R., Ji, S., Zheng, X., et al. (2019). Bismuth single atoms resulting from transformation of metal-organic frameworks and their use as electrocatalysts for CO_2 reduction. J. Am. Chem. Soc. *141*, 16569–16573. https://doi.org/10.1021/jacs.9b08259.

Zhang, H., Wei, J., Dong, J., Liu, G., Shi, L., An, P., Zhao, G., Kong, J., Wang, X., Meng, X., et al. (2016). Efficient visible-light-driven carbon dioxide reduction by a single-atom implanted metal-organic framework. Angew. Chem. Int. Ed. *55*, 14310–14314. https://doi.org/10.1002/anie.201608597.

Zhang, J., Zheng, C., Zhang, M., Qiu, Y., Xu, Q., Cheong, W.-C., Chen, W., Zheng, L., Gu, L., Hu, Z., et al. (2020a). Controlling N-doping type in carbon to boost single-atom site Cu catalyzed transfer hydrogenation of quinoline. Nano Res. *13*, 3082–3087. https://doi.org/10.1007/s12274-020-2977-4.

Zhang, N., Ye, C., Yan, H., Li, L., He, H., Wang, D., and Li, Y. (2020b). Single-atom site catalysts for environmental catalysis. Nano Res. *13*, 3165–3182. https://doi.org/10.1007/s12274-020-2994-3.

Zhang, J.-H., Yang, W., Zhang, M., Wang, H.-J., Si, R., Zhong, D.-C., and Lu, T.-B. (2021a). Metal-organic layers as a platform for developing single-atom catalysts for photochemical CO_2 reduction. Nano Energy *80*, 105542. https://doi.org/10.1016/j.nanoen.2020.105542.

Zhang, N., Zhang, X., Kang, Y., Ye, C., Jin, R., Yan, H., Lin, R., Yang, J., Xu, Q., Wang, Y., et al. (2021b). A supported Pd2 dual-atom site catalyst for efficient electrochemical CO_2 reduction. Angew. Chem. Int. Ed. *60*, 13388–13393. https://doi.org/10.1002/anie.202101559.

Zhang, N., Zhang, X., Tao, L., Jiang, P., Ye, C., Lin, R., Huang, Z., Li, A., Pang, D., Yan, H., et al. (2021c). Silver single-atom catalyst for efficient electrochemical CO_2 reduction synthesized from thermal transformation and surface reconstruction. Angew. Chem. Int. Ed. *60*, 6170–6176. https://doi.org/10.1002/anie.202014718.

Zhang, X., Fan, Y., You, E., Li, Z., Dong, Y., Chen, L., Yang, Y., Xie, Z., Kuang, Q., and Zheng, L. (2021d). MOF encapsulated sub-nm Pd skin/Au nanoparticles as antenna-reactor plasmonic catalyst for light driven CO_2 hydrogenation. Nano Energy *84*, 105950. https://doi.org/10.1016/j.nanoen.2021.105950.

Zhao, C., Dai, X., Yao, T., Chen, W., Wang, X., Wang, J., Yang, J., Wei, S., Wu, Y., and Li, Y. (2017). Ionic exchange of metal-organic frameworks to access single nickel sites for efficient electroreduction of CO_2. J. Am. Chem. Soc. *139*, 8078–8081. https://doi.org/10.1021/jacs.7b02736.

Zhao, W., Li, G., and Tang, Z. (2019). Metal-organic frameworks as emerging platform for supporting isolated single-site catalysts. Nano Today *27*, 178–197. https://doi.org/10.1016/j.nantod.2019.05.007.

Zhao, Y., Zheng, L., Jiang, D., Xia, W., Xu, X., Yamauchi, Y., Ge, J., and Tang, J. (2021). Nanoengineering metal-organic framework-based materials for use in electrochemical CO_2 reduction reactions. Small *17*, e2006590. https://doi.org/10.1002/smll.202006590.

Zhao, K., Nie, X., Wang, H., Chen, S., Quan, X., Yu, H., Choi, W., Zhang, G., Kim, B., and Chen, J.G. (2020a). Selective electroreduction of CO_2 to acetone by single copper atoms anchored on N-doped porous carbon. Nat. Commun. *11*, 2455. https://doi.org/10.1038/s41467-020-16381-8.

Zhao, Y., Zhou, S., and Zhao, J. (2020b). Selective C-C coupling by spatially confined dimeric metal centers. iScience *23*, 101051. https://doi.org/10.1016/j.isci.2020.101051.

Zhou, Y., Zheng, L., Yang, D., Yang, H., Lu, Q., Zhang, Q., Gu, L., and Wang, X. (2021a). Enhancing CO_2 electrocatalysis on 2D

porphyrin-based metal-organic framework nanosheets coupled with visible-light. Small Methods *5*, e2000991. https://doi.org/10.1002/smtd.202000991.

Zhou, Z., Li, M., Kuai, C., Zhang, Y., Smith, V.F., Lin, F., Aiello, A., Durkin, D.P., Chen, H., and Shuai, D. (2021b). Fe-based single-atom catalysis for oxidizing contaminants of emerging concern by activating peroxides. J. Hazard. Mater. *418*, 126294. https://doi.org/10.1016/j.jhazmat.2021.126294.

Zhu, J., Shao, W., Li, X., Jiao, X., Zhu, J., Sun, Y., and Xie, Y. (2021). Asymmetric triple-atom sites confined in ternary oxide enabling selective CO_2 photothermal reduction to acetate. J. Am. Chem. Soc. *143*, 18233–18241. https://doi.org/10.1021/jacs.1c08033.

Zhuang, Z., Kang, Q., Wang, D., and Li, Y. (2020). Single-atom catalysis enables long-life, high-energy lithium-sulfur batteries. Nano Res. *13*, 1856–1866. https://doi.org/10.1007/s12274-020-2827-4.

Zou, L., Wei, Y.S., Hou, C.C., Li, C., and Xu, Q. (2021). Single-atom catalysts derived from metal-organic frameworks for electrochemical applications. Small *17*, e2004809. https://doi.org/10.1002/smll.202004809.